npj | parkinson's disease

Article

Published in partnership with the Parkinson's Foundation

https://doi.org/10.1038/s41531-026-01281-3

LRRK2^{R1627P} mutation amplifies environmental risk factors induced chronic inflammation and α-synuclein aggregation in the gut of rats

Shimin Pang[1], Jing Lu[1,2], Yanyan Wang[1], Chao Ying[1], Chunsong Zhao[1], Zhenyu Yue[3], Qiumei Yang[1,2] ✉ & Piu Chan[1,2,4,5] ✉

Chronic intestinal inflammation is a key precursor to Parkinson's disease (PD). Leucine-rich repeat kinase 2 R1628P variant (LRRK2^{R1628P}) is a risk factor for PD in Asians. However, whether it drives the occurrence of intestinal inflammation remains elusive. Here, we report that LRRK2^{R1627P} (the rat homolog) disrupts intestinal homeostasis during aging and toxin exposure in rats. Compared with age-matched wild-type rats, aging LRRK2^{R1627P} rats exhibited shortened small intestine, reduced goblet cells, and abnormal epithelial cell junction structures. Mechanistically, these changes were induced by macrophage polarization toward a pro-inflammatory phenotype via TLR4/MyD88/NF-κB pathway, resulting in PD-associated intestinal pathology, including chronic inflammatory, decreased microbial diversity, and increased p-α-synuclein aggregation. LRRK2^{R1627P} also enhanced susceptibility to lipopolysaccharide-induced intestinal inflammation. Remarkably, TLR4 inhibitor ameliorated the age-related disruption of intestinal homeostasis mediated by LRRK2^{R1627P}. Using the LRRK2^{R1627P} rats, this study reveals a cascading interplay among genetic susceptibility, age-related internal imbalance, and exogenous toxin exposure in PD pathology. These findings provide critical insights into how the dynamic interplay of multiple risk factors overwhelms the body's compensatory thresholds, ultimately initiating the pathological process of neurodegeneration.

The intestine is a highly dynamic tissue that continuously regenerates, crucial for maintaining host health and regulating aging. Intestinal inflammation has been identified as a critical gastrointestinal feature of Parkinson's disease (PD), characterized by disturbed microbial environment, damaged epithelial integrity, abnormal immune response and elevated levels of pro-inflammatory markers in the gut of PD patients[1–5]. Toll-like receptor 4 (TLR4), as a primary interface between the external microbial environment and internal biological functions, plays a central role in mediating gene-environment interactions and the development of intestinal inflammation[6–8]. TLR4 initiates signaling cascades by recognizing specific pathogen-associated molecular patterns (PAMPs) or damage-associated molecular patterns (DAMPs). This leads to the release of inflammatory cytokines, contributing to compromised epithelial barrier integrity and the development of localized inflammation. Therefore, focusing on the immune system dysregulation mediated by TLR4 is essential for understanding the development and treatment of intestinal inflammation.

Leucine-rich repeat kinase 2 (LRRK2) is implicated in both hereditary and sporadic PD[9–11], and is also a risk gene for Crohn's disease (CD)[12–14]. Although the pathogenesis of LRRK2-related intestinal inflammation remains unclear, the high expression of LRRK2 in innate immune cells suggests its role in regulating innate immune-related inflammatory pathways[15]. In the dextran sulfate sodium salt (DSS) colitis model, the

[1]Department of Neurobiology and National Clinical Research Center for Geriatric Disease, Xuanwu Hospital of Capital Medical University, Beijing Institute of Geriatrics, Beijing, China. [2]Advanced Innovation Center for Human Brain Protection, Capital Medical University, Beijing, China. [3]Department of Neurobiology, Icahn School of Medicine at Mount Sinai, New York, NY, USA. [4]Clinical and Research Center for Parkinson's Disease, Capital Medical University, Key Laboratory for Neurodegenerative Disease of the Ministry of Education, Beijing Key Laboratory for Parkinson's Disease, Beijing, China. [5]Beijing Institute of Brain Disorders, Collaborative Innovation Center for Brain Disorders, Capital Medical University, Beijing, China.
✉e-mail: qmyang@xwhosp.org; pbchan@hotmail.com

increased intestinal permeability and loss of enteric nerve fibers caused by the LRRK2^{G2019S} mutation are attributed to the activation of TLR4, an innate immune component functioning as a pattern recognition receptor, which subsequently triggers an enhanced inflammatory response mediated by the downstream NF-κB pathway[16]. Studies have demonstrated that the activated TLR4/NF-κB signaling pathway regulates the polarization of macrophages towards pro-inflammatory phenotype and the release of interleukin-6 (IL-6), inducible nitric oxide synthase (iNOS), and tumor necrosis factor-α (TNF-α), which contribute to the development of intestinal inflammation[17–19]. In vitro, LRRK2 can regulate the recruitment and polarization of macrophages[20,21]. Recently, Jing Yan et al. reported that LRRK2^{R1441C} mutation promotes macrophage polarization, as well as the secretion of IL-6 and TNF-α, thereby exacerbating the progression of colitis in mice[22]. It therefore stands to reason that the infiltration of pro-inflammatory macrophages and the secretion of inflammatory factors triggered by TLR4 activation are critical for the LRRK2-mediated development of intestinal inflammation.

In recent years, the theory that the abnormal aggregation of α-synuclein (α-Syn), a pathological hallmark of PD, originates from the intestine has garnered significant attention[23]. The activation of immune cells and the release of pro-inflammatory factors gradually create a chronic inflammatory environment in the intestine, which is considered an important incentive for the development of pathological α-Syn[24]. It has reported that LRRK2 can phosphorylate recombinant α-Syn at serine-129[25]. Given the current evidence that LRRK2 regulates immune responses and α-Syn phosphorylation, it is reasonable to speculate that LRRK2-related immune responses may contribute to the expression of pathological α-Syn. Additionally, animal studies have provided intriguing clues that abnormal α-Syn expression can be induced by LRRK2-mediated dysbiosis[26,27]. Collectively, these findings suggest that the crosstalk between LRRK2-mediated immune responses, the microbiome, and pathological α-Syn may represent an early event and a potential danger signal in PD.

LRRK2^{R1628P} has been identified as a risk factor for PD in the Chinese population[28]. However, whether the LRRK2^{R1628P} mutation is associated with intestinal inflammation and PD pathology remains unclear. The current study utilized LRRK2^{R1627P} rats (equivalent to human LRRK2^{R1628P}) to investigate whether the LRRK2^{R1627P} mutation influences the TLR4 signaling pathway and macrophage-mediated innate immune responses, thereby triggering chronic inflammation and abnormal p-α-Syn expression in the gut during aging. Additionally, we assessed the intervention of a TLR4 inhibitor on the intestinal immune response, microbiome composition, and pathological α-Syn expression in LRRK2^{R1627P} rats. This study suggests that, against the backdrop of interactions among genetic factors, aging, and environmental toxins, LRRK2-realted inflammation and abnormal expression of p-α-Syn in the gut may represent early events in the pathological development of PD, providing a new perspective for exploring early intervention strategies for PD.

Results

Expression of LRRK2 in the small intestine of LRRK2^{R1627P} rats

Immunofluorescence staining was performed to characterize the distribution of LRRK2 in the small intestine of WT rats. As shown in Fig. 1a, LRRK2^{+} cells were mainly localized in the lamina propria (LP) and co-expressed with βIII-Tubulin (a neuronal marker) in the myenteric plexus. Next, we quantified the endogenous expression levels of LRRK2. The qPCR results showed that the mRNA levels of LRRK2 in the small intestine of LRRK2^{R1627P} rats remained consistent with those of WT rats, even in old age (Fig. 1b). Additionally, we assessed the protein levels of LRRK2 and its major substrates, Rab GTPases, in the small intestine of rats at different age. According to the western blot analysis, it was observed that the protein levels of total LRRK2 were significantly reduced, but the phosphorylation level of LRRK2 at S935 showed no significant changes in LRRK2^{R1627P} rats compared with age-matched WT rats after normalizing against the total LRRK2 protein (Fig. 1c). However, the phosphorylation level of Rab10 at T73 was significantly reduced, but the phosphorylation level of Rab8a at T72 showed no significant changes (Fig. 1d). We also examined the expression of other substrates of LRRK2, Rab2 and Rab5a, and the results showed that their expression was not significantly different among the three groups of rat small intestines (Fig. 1d). Therefore, the LRRK2^{R1627P} mutation results in a notably reduction of total LRRK2 protein expression, as well as a decrease in the phosphorylation level of Rab10 at T73 in the small intestine of rats, while the LRRK2 mRNA levels remain unchanged.

Intestinal physiopathological characteristics of LRRK2^{R1627P} rats

We measued the full length of the small intestin in rats at differnet ages. There was no statistical difference in the length of the small intestine between the three groups of rats at 2 months. However, from 8 months of age, LRRK2 transgenic rats (LRRK2^{R1627P} rats and LRRK2$^{-/-}$ rats) had shorter small intestine compared with age-macthed WT rats (Fig. 2a). Our previous studies showed that LRRK2 transgenic rats exhibited significantly lower body weight than WT rats with aging, although their defecation habits showed no significant changes throughout their lifespan[29]. We hypothesize that this may be related to functional alterations in the small intestine, which is responsible for digestion and absorption. Given that the jejunum is the primary site for nutrient absorption, this study focuses on the proximal jejunum (sampling location shown in Fig. 2b).

Following the guideline for histological evaluation of intestinal inflammation published by Ulrike Erben et al.[30], we assesed the pathological phenotype of jejunum in the three groups of rats at different ages in terms of inflammatory cell infiltration, epithelial changes and mucosal structure. The Fig. 2c showed that there was no overt sign of lymphoid aggregates in the LP, mucosa, submucosa, or muscular layer; and no obvious epithelial changes such as crypt hyperplasia, cryptitis, crypt abscess, or surface epithelial loss were found. The mucosal structure remained intact, without significant ulcers, granulation tissue, or villous atrophy. However, from 8 months of age, LRRK2 transgenic rats exhibited lower villus height and crypt depth compared with age-matched WT rats (Fig. 2c, d). This phenomenon was also observed in the ileum of aged rats (Supplementary Fig. S2a). However, there were no significant differences in the pathological phenotypes of the colon among the three groups of rats (Supplementary Fig. S2b). Then we conducted immunohistochemical staining to evaluate intestinal proliferation and apoptosis. It was observed that, from 8 months of age, the number of Ki67^{+} (a proliferation marker) cells in the crypts of LRRK2 transgenic rats was approximately two-thirds of that in age-matched WT rats (Fig. 2e). Labeling apoptotic cells with anti-Cleaved caspase 3 antibody, no significant difference was found in the number of deeply stained apoptotic cells at the tips of villi among the three groups of rats (Fig. 2f). To summarize, LRRK2^{R1627P} and LRRK2$^{-/-}$ rats did not show significant pathological alterations in intestinal architecture throughout their lifetimes. However, with advancing age, their intestinal proliferative capacity was observed to be lower compared with age-matched WT rats.

IECs differentiation and junctions in the small intestine of LRRK2^{R1627P} rats

The diversity of intestinal epithelial cells (IECs) is crucial for maintaining intestinal homeostasis. We examined the expression of major secretory IECs, goblet cells and Paneth cells, as well as absorptive IECs, enterocytes, in the three groups of rats during development. The AB-PAS staining showed no significant difference in the number of mucin-secreting goblet cells among the three groups of rats at 2 and 8 months of age. However, at 16 months of age, both LRRK2^{R1627P} and LRRK2$^{-/-}$ rats exhibited a noticeable reduction in the number of goblet cells compared with age-matched WT rats. This tendency continued to worsen with age (Fig. 3a). Using lysozyme as a marker, we observed a significant decrease in the number of Paneth cells in the crypts of LRRK2 transgenic rats from 2 months of age (Fig. 3b). Then we quantified the protein levels of MUC2 (goblet cells maker) and Villin (enterocytes marker). At 16 and 20–22 months of age, LRRK2^{R1627P} rats had significantly lower MUC2 protein levels in the small intestine than age-matched WT rats, and the decrease was more pronounced in LRRK2$^{-/-}$ rats. The Villin protein levels

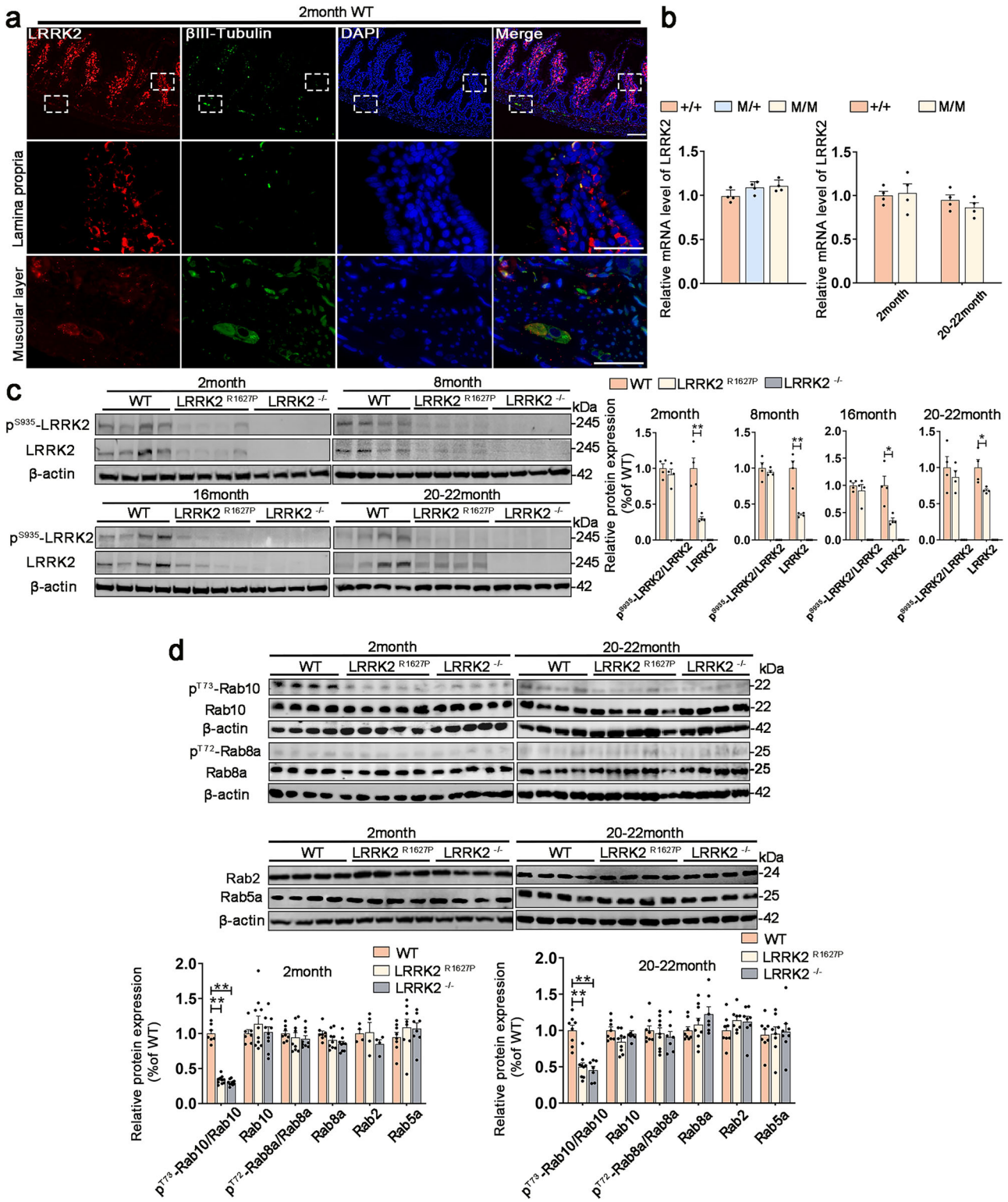

Fig. 1 | Expression of LRRK2 in the rat small intestine. a Paraffin sections of 2-month-old WT rat small intestine immunolabeled with anti-LRRK2 antibody (red) and anti-βIII-Tubulin antibody (green). Nuclei were stained with DAPI (blue). The upper panels show the overall distribution of LRRK2 under low magnification, the middle panels show the localization of LRRK2 in the LP under high magnification, and the lower panels show the localization of LRRK2 in the myenteric plexus under high magnification. Scale bar 100 μm. **b** qPCR analysis of LRRK2 mRNA levels in the small intestine of WT rats (+/+), LRRK2^{R1627P} heterozygous mutant rats (M/+) and LRRK2^{R1627P} homozygous mutant rats (M/M), $n = 4$. **c**, **d** Western blot analysis for p^{S935}-LRRK2, total LRRK2 ($n = 4$), p^{T73}-Rab10, total Rab10, p^{T72}-Rab8a, total Rab8a, Rab2 and Rab5a ($n = 4$–10) protein levels in the small intestine of WT rats, LRRK2^{R1627P} rats (all of the following experiments were performed on LRRK2^{R1627P} homozygous mutant rats) and LRRK2$^{-/-}$ rats at indicated ages. Data are presented as mean ± SEM; one-way ANOVA or Student's t test was used; $^{*}p < 0.05$, $^{**}p < 0.01$.

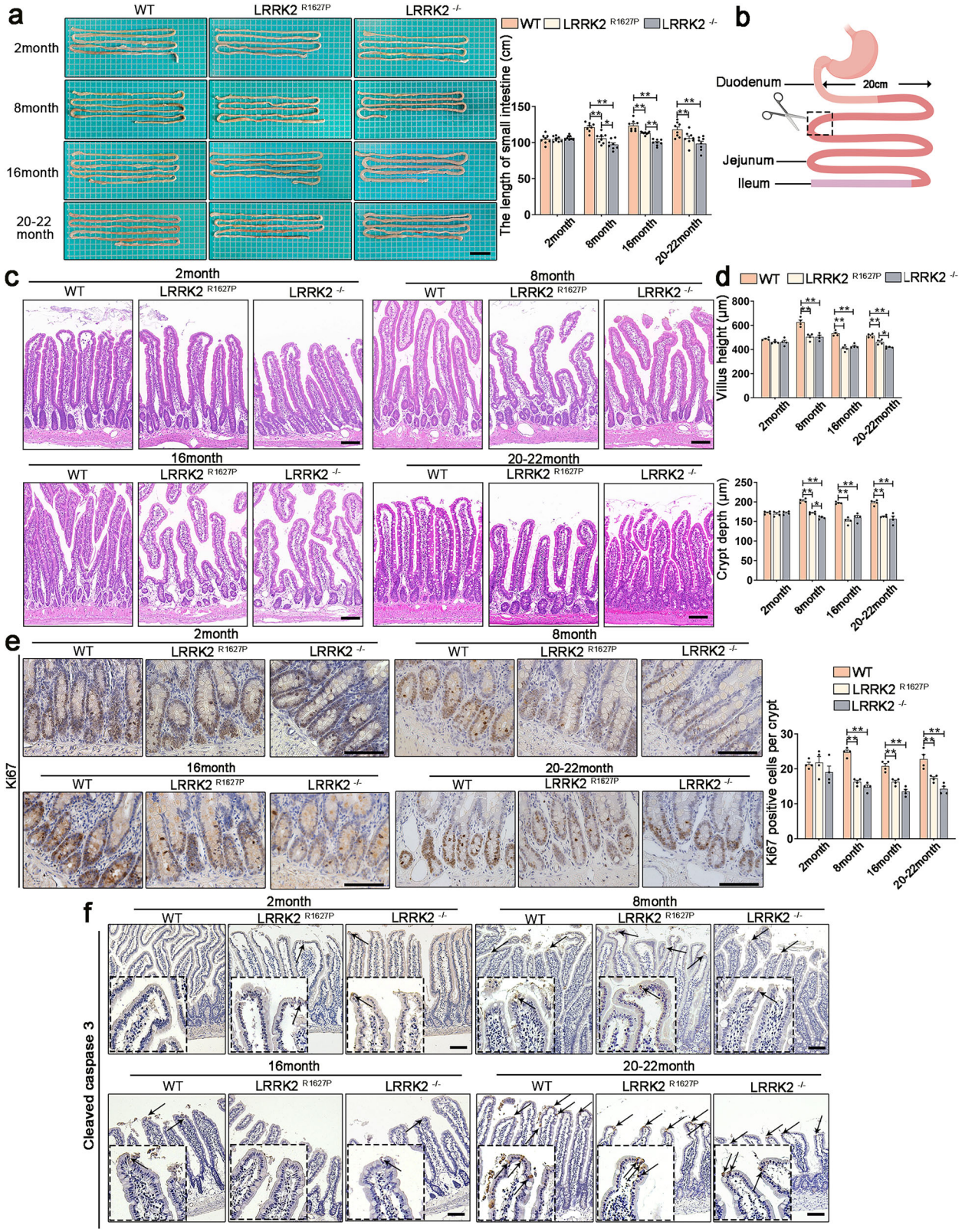

Fig. 2 | Intestinal pathological phenotypes of WT, LRRK2^{R1627P} and LRRK2$^{-/-}$ rats at different ages. a Measurement of small intestine length. Scale bar 5 cm, $n = 8$. Two-way ANOVA was used; interaction $p < 0.0001$. **b** Schematic diagram of the sampling site. The term "small intestine" used in this study refers to the proximal jejunum tissue. **c** HE staining images of the small intestine. Scale bar 100 μm, $n = 4$. **d** Measurement of villus height and crypt depth in the small intestine, $n = 4$. Two-way ANOVA was used; interaction $p < 0.0001$. **e** Immunohistochemical staining images of Ki67 in the small intestine, and the quantification of Ki67 positive cells in the crypts (determined based on the number of brown-stained cell nuclei in the crypts). Scale bar 100 μm, $n = 4$. Two-way ANOVA was used; interaction $p < 0.01$. **f** Immunohistochemical staining images of Cleaved-caspase 3 in the small intestine, and the quantification of Cleaved-caspase 3 positive cells in the villus. Arrows show the apoptotic cells. Scale bar 100 μm, $n = 4$. Two-way ANOVA was used; interaction $p > 0.05$. Data are presented as mean ± SEM, $^{*}p < 0.05$, $^{**}p < 0.01$.

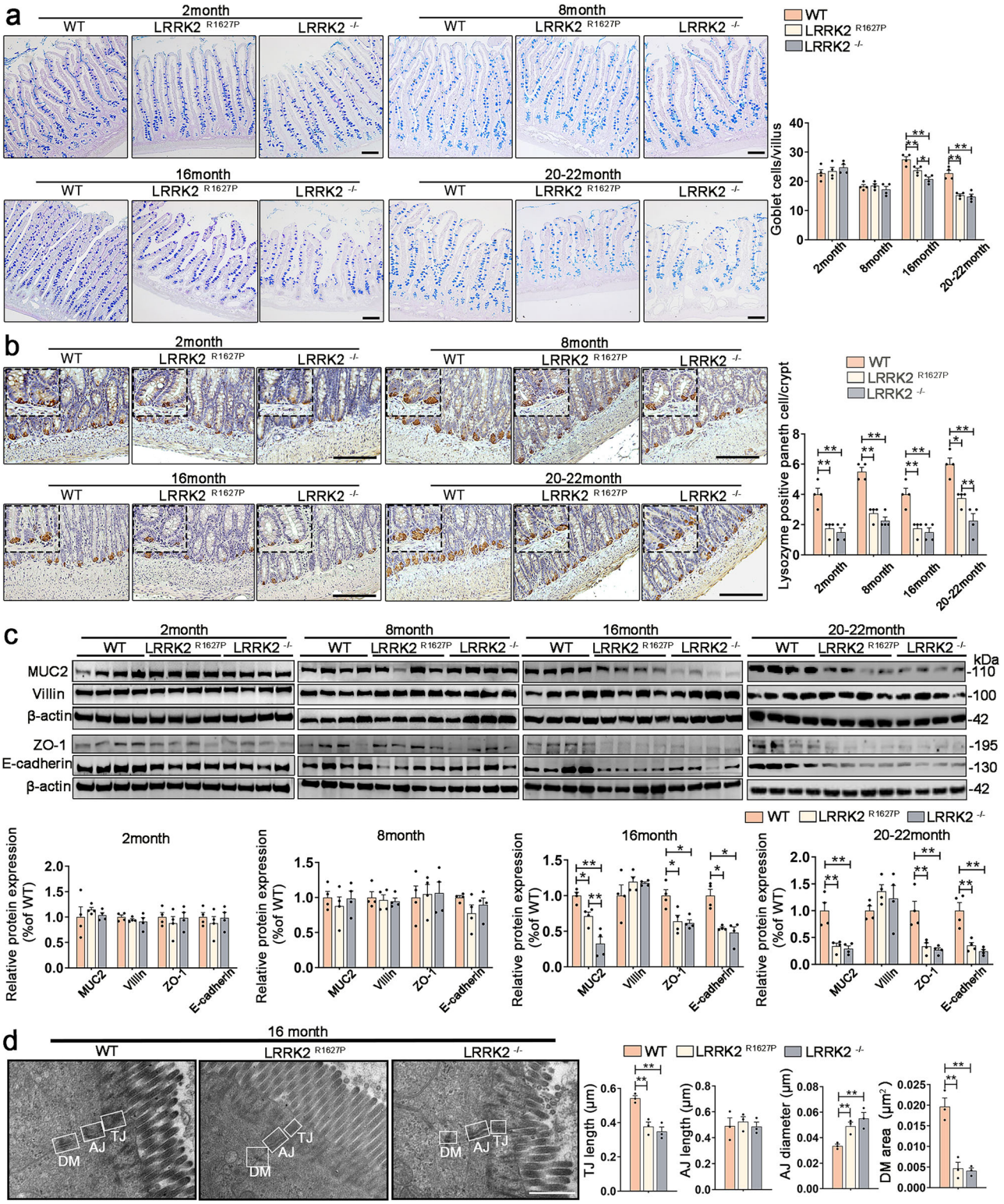

Fig. 3 | Differentiation and intercellular junctions of small intestinal epithelial cells in rats at different ages. a Images of AB-PAS stained goblet cells and statistical analysis of goblet cell numbers in the small intestine. Scale bar 100 μm, $n = 4$. Two-way ANOVA was used; interaction $p < 0.0001$. **b** Immunohistochemical staining images of lysozyme and the quantification of lysozyme positive cells in the crypts. Scale bar 100 μm, $n = 4$. Two-way ANOVA was used; interaction $p > 0.05$. **c** Western blot analysis for MUC2, Villin, ZO-1 and E-cadherin protein levels in the small intestine of WT, LRRK2^{R1627P} and LRRK2$^{-/-}$ rats at indicated ages, $n = 4$. One-way ANOVA was used. **d** TEM images of epithelial intercellular junctions in the small intestine from 16-month-old WT, LRRK2^{R1627P} and LRRK2$^{-/-}$ rats, as well as statistical analysis of small intestinal TJ length, AJ length, AJ diameter and DM area. Scale bar 1 μm, $n = 3$. One-way ANOVA was used. Data are presented as mean ± SEM, $^{*}p < 0.05$, $^{**}p < 0.01$.

were not significantly different (Fig. 3c, Supplementary Fig. S3). The close arrangement between IECs forms a junctional complex that includes tight junction (TJ), adherens junction (AJ) and desmosome (DM) located below the base of microvilli. This complex plays a crucial role in maintaining the integrity of the intestinal barrier. Western blot results showed a substantial reduction in the protein levels of ZO-1 (a member of TJ families) and E-cadherin (a member of AJ families) in the small intestine of LRRK2 transgenic rats as compared with age-matched WT rats (Fig. 3c, Supplementary Fig. S3). The ultramorphological structure of the intestinal epithelium in 16-month-old rats was observed by TEM. As shown in Fig. 3d, there was no significant loss of TJ, AJ, DM structures or bubble-like openings between adjacent cells in the small intestine of WT, LRRK2^{R1627P} and LRRK2$^{-/-}$ rats. However, in the LRRK2^{R1627P} and LRRK2$^{-/-}$ groups, the length of TJ and the electron-dense area of DM were significantly reduced, while the diameter of AJ was significantly increased compared with WT group. Collectively, LRRK2^{R1627P} or LRRK2$^{-/-}$ affects the differentiation of goblet cells and the intercellular junctions of IECs in an age-dependent manner.

TLR4/NF-κB pathway and p-α-Syn aggregation in the small intestine of LRRK2^{R1627P} rats

To explore the mechanisms underlying intestinal homeostasis disruption in LRRK2 transgenic rats, we performed mRNA sequencing analysis on total RNA isolated from the small intestine of rats at 16 months of age. Transcriptome analysis revealed 1132 significantly differentially expressed genes (DEGs) in LRRK2^{R1627P} vs WT, consisting of 569 upregulated DEGs and 563 downregulated DEGs. In LRRK2$^{-/-}$ vs WT, there were 754 significantly different DEGs, consisting of 379 upregulated DEGs and 375 downregulated DEGs (Fig. 4a). To identify potential biological functions and signaling pathways, we performed Gene Ontology (GO) enrichment analysis and Kyoto Encyclopedia of Genes and Genomes (KEGG) pathway analysis on these DEGs. The Biological Process (BP) category in GO enrichment indicated significant enrichment of functions related to inflammation and immunity in LRRK2 transgenic rats compared with WT rats, such as response to stimulus, immune system process, and immune response. Furthermore, KEGG pathway analysis of DEGs in the BP category revealed significant enrichment of the NF-κB signaling pathway and Toll-like receptor signaling pathway in LRRK2 transgenic rats (Fig. 4b, c). After quantifying TLR4, MyD88 and NF-κB protein levels by western blot, it was confirmed that TLR4/MyD88/NF-κB pathway was overactived in the small intestine of LRRK2 transgenic rats than in age-matched WT rats at 16 and 20–22 months of age (Fig. 4d, Supplementary Fig. S4a, b). We also evaluated the subcellular localization of NF-κB p65. As shown in Supplementary Fig. S4c, d, compared with WT rats, the expression of NF-κB p65 in both the nucleus and cytoplasm was significantly increased in LRRK2 transgenic rats.

Based on TEM, we found that the immune cells in the LP of 16-month-old LRRK2 transgenic rats were more abundant than those in WT rats (Fig. 4e). Considering that TLR4 is a crucial pattern recognition receptor in the innate immune system and the activation of the TLR4/NF-κB signaling pathway has been shown to play a key role in regulating the function of innate immune cells, particularly macrophages[31], we have focused on macrophage polarization. Macrophages can be described as M1 or classically activated or pro-inflammatory macrophages, and M2 or alternatively activated or anti-inflammatory macrophages. In rats, M1 and M2 macrophages are identifiable by CD68 and CD163, respectively[32]. We then assessed the compositional differences between M1 and M2 macrophages in rats at different ages. Western blot results revealed consistent protein level of CD68 or CD163 in the small intesinte for all three groups of rats at 2 and 8 months of age (Supplementary Figs. S4b, S5a, S5b). At 16 and 20–22 months of age, the LRRK2 transgenic rats exhibited a significantly higher expression of CD68 compared with the age-matched WT rats, while the expression of CD163 did not display significant alterations (Fig. 4f, Supplementary Fig. S5a, b). Immunofluorescence revealed that starting from 16 months of age, the number of CD68$^+$ cells in the LP of LRRK2 transgenic rats was significantly higher than that in WT rats (Fig. 4g, k, Supplementary Fig. S6a, d). Flow cytometry was used to quantify macrophages in the LP of rats at 16 and 20-22 months of age. Our results showed that CD11b$^+$ total macrophages were more aboundant in the LP of LRRK2 transgenic rats than in WT rats. Macrophage subtype analysis revealed a significant increase in the percentage of M1 cells in LRRK2 transgenic rats compared with WT rats, while the percentage of M2 cells showed no statistical difference (Fig. 4h, i, Supplementary Fig. S5c, d). Notably, multiplex immunofluorescence staining revealed that TLR4 expression in the gut was predominantly localized to CD68$^+$ cells (Supplementary Fig. S7). M1 macrophages typically exhibit pro-inflammatory effects as a result of the overexpression of mediators such as inducible Nitric Oxide Synthase (iNOS), IL-1β, IL-6, IL-12, IL-23 and TNF-α[33]. We examined the expression of iNOS and IL-6 in the small intestine. At the 16 and 20-22 months of age, the expression of iNOS and IL-6 was significantly increased in LRRK2 transgenic rats compared with WT rats of the same age, this phenomenon was not observed in 2-month-old and 8-month-old rats (Fig. 4g, k, Supplementary Fig. S6b, d).

The chronic inflammatory environment in the gut has been suggested to be a key factor in inducing the abnormal expression of α-Syn. Our previous studies found a significant increase in p-α-Syn expression in the small intestine of LRRK2 transgenic rats starting from 16 months of age[29]. In this study, we further examined the distribution of p-α-Syn at different ages. Notably, p-α-Syn was not aggregated in the neurons of the myenteric plexus, but was primarily expressed in CD68$^+$ cells within the LP (Supplementary Fig. S8). Furthermore, the expression of p-α-Syn in CD68$^+$ macrophages sharply increased in the LP of the jejunum of 16 and 20-22-month-old LRRK2 transgenic rats compared with age-matched WT rats (Fig. 4j, k, Supplementary Fig. S6c, d). Aberrant p-α-Syn expression was also observed in the ileum, while it was absent in the colon (Supplementary Fig. S2c, d). These findings suggest that LRRK2^{R1627P} or LRRK2$^{-/-}$ leads to the formation of a pro-inflammatory environment in the rat small intestine in an age-dependent manner. Overactivation of the innate immune system characterized by increased expression of TLR4/MyD88/NF-κB pathway and M1 macrophages results in pathological α-Syn accumulation in the small intestine of LRRK2 transgenic rats.

Effects of environmental stimulus LPS on small intestinal homeostasis of LRRK2^{R1627P} rats

Then we intraperitoneally injected the TLR4 agonist LPS in 2-month-old rats (at an age where there were no discernible variations in TLR4 pathway among the three groups of rats) to assess the ability of LRRK2 to regulate intestinal homeostasis in response to environmental stimulus. HE staining showed that LRRK2 transgenic rats exhibited more severe shedding of IECs and mass infiltration of inflammatory cells in the LP compared with WT rats. Increased red blood cells were found in the LP of LRRK2^{R1627P} rats, which was further intensified in LRRK2$^{-/-}$ rats (Fig. 5a, Supplementary Fig. S9a). In addition, the goblet cells in LRRK2 transgenic rats migrated upwards more slowly and more goblet cells were present in the crypt than in WT rats following LPS stimulation (Fig. 5b). After staining with anti-Cleaved caspase 3 antibody, LRRK2 transgenic rats showed increased labeled apoptotic IECs at the tips of villi (Fig. 5c, Supplementary Fig. S9b). Western blot results showed the expression levels of ZO-1 and E-cadherin were decreased, while the expression levels of TLR4, MyD88, NF-κB and CD68 were increased in LRRK2 transgenic rats when exposed to LPS (Fig. 5d, Supplementary Fig. S9e, f). Compared with WT rats, LPS significantly increased the expression of NF-κB p65 in LRRK2 transgenic rats, both in the cytoplasm and the nucleus (Fig. S9g). Consistent with the western blot results, the number of CD68$^+$ cells in the LP were significantly greater in LRRK2 transgenic rats, whereas the number of CD163$^+$ cells showed no statistical difference after LPS treatment. The fluorescence signal intensities of iNOS and IL-6 in the LP of LRRK2 transgenic rats were also

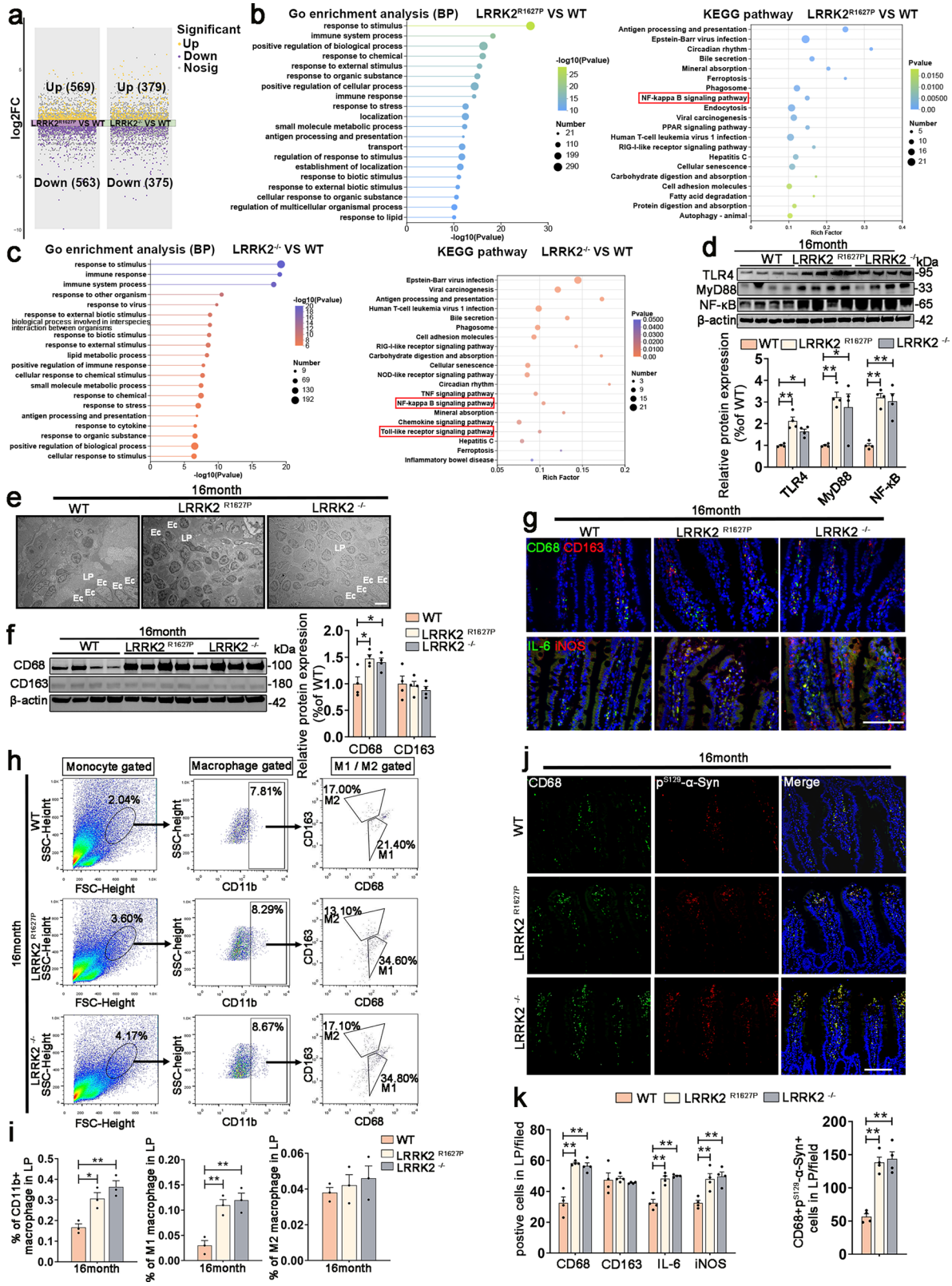

stronger than that in WT rats (Fig. 5e, Supplementary Fig. S9c). As anticipated, abnormal aggregation of p-α-Syn was identified in activated pro-inflammatory macrophages induced by LPS exposure in LRRK2 transgenic rats LP (Fig. 5e, Supplementary Fig. S9d). Taken together, LRRK2^{R1627P} or LRRK2$^{-/-}$ amplified the rats' sensitivity towards environmental stimulus LPS-induced acute intestinal inflammation.

Effects of TLR4 inhibitor on small intestinal pathology of LRRK2^{R1627P} rats

Considering the significantly increased TLR4 signal and disrupted intestinal homeostasis in the LRRK2 transgenic rats from 16 months of age, TLR4-targeted inhibitor was administered to rats from 8 to 16 months of age to evaluate its potential effects on the reversal of intestinal homeostasis.

Fig. 4 | Innate immune response and pathological α-Syn aggregation in the small intestine of 16-month-old rats. a Volcano plot comparing DEGs for RNA-seq in LRRK2^{R1627P} vs WT, LRRK2$^{-/-}$ vs WT (p value < 0.05, fold change >1.2), $n = 3$. **b** BP categories in GO enrichment analysis and KEGG pathway of DEGs in LRRK2^{R1627P} vs WT, $n = 3$. **c** BP categories in GO enrichment analysis and KEGG pathway of DEGs in LRRK2$^{-/-}$ vs WT, $n = 3$. **d** Western blot analysis for TLR4, MyD88 and NF-κB protein levels in the small intestine of rats, $n = 4$. One-way ANOVA was used. **e** TEM images of rats small intestinal LP. Ec enterocytes, LP lamina propria. Scale bars 5 μm, $n = 3$. One-way ANOVA was used. **f** Western blot analysis for CD68 and CD163 protein levels in the small intestine of rats, $n = 4$. One-way ANOVA was used. **g** Immunofluorescence staining images of CD68 (green) and CD163 (red) (upper panel), IL-6 (green) and iNOS (red) (down panel) positive cells in the small intestinal LP of rats. Nuclei were stained with DAPI (blue). Scale bar 100 μm, $n = 4$. One-way ANOVA was used. **h** Flow cytometry scatter plot of small intestianl LP isolated from rats, $n = 3$. CD11b$^+$CD68$^+$CD163$^-$ cells represent M1 population and CD11b$^+$CD68$^-$CD163$^+$ cells represent M2 population. **i** Statistical analysis of total macrophages, M1 macrophages and M2 macrophages in the small intestianl LP using flow cytometry. One-way ANOVA was used. **j** Immunofluorescence staining images of CD68 (green) and p^{S129}-α-Syn (red) positive cells in the small intestinal LP of rats. Nuclei were stained with DAPI (blue). Scale bar 100 μm, $n = 4$. **k** Statistical analysis of immunofluorescence staining. One-way ANOVA was used. Data are presented as mean ± SEM, $^*p < 0.05$, $^{**}p < 0.01$.

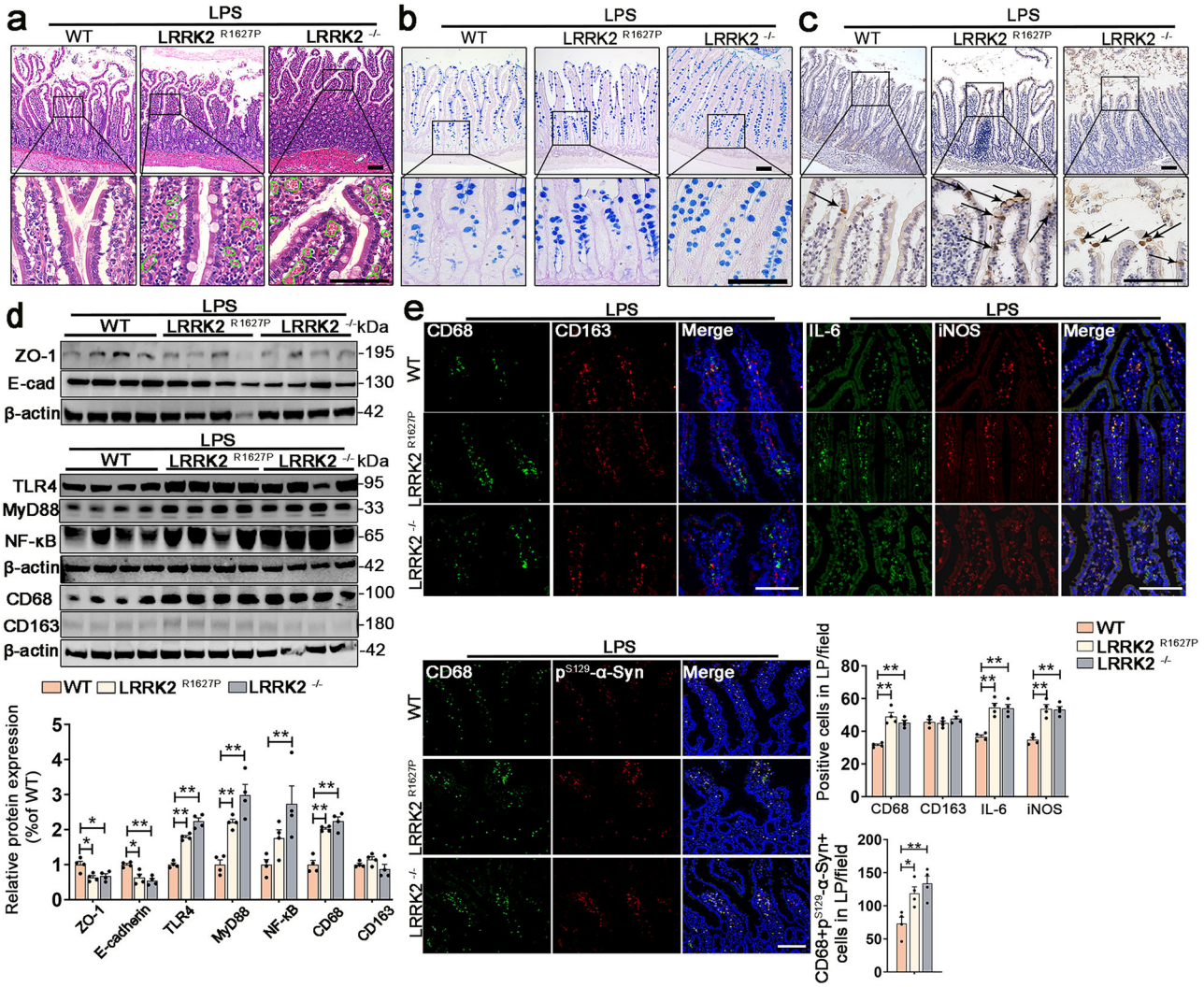

Fig. 5 | Effect of intraperitoneal injection of LPS on rat small intestine after 6 h. a HE staining images of the small intestine of LPS-treated rats. The green circles in the lower panels highlight the red blood cells in the LP. Scale bar 100 μm, $n = 4$. **b** Images of goblet cells stained with AB-PAS in the small intestine of LPS-treated rats. Scale bar 100 μm, $n = 4$. **c** Immunohistochemical staining images of Cleaved caspase 3 in the small intestine of LPS-treated rats. Arrows show apoptotic IECs. Scale bar 100 μm, $n = 4$. **d** Western blot analysis for ZO-1, E-cadherin, TLR4, MyD88, NF-κB, CD68 and CD163 protein levels in the small intestine of LPS-treated rats, $n = 4$. **e** Immunofluorescence staining images and quantification of CD68/IL-6 (green) and CD163/iNOS/p^{S129}-α-Syn (red) positive cells in the small intestinal LP of LPS-treated rats. Nuclei were stained with DAPI (blue). Scale bar 100 μm, $n = 4$. One-way ANOVA was used. Data are presented as mean ± SEM, $^*p < 0.05$, $^{**}p < 0.01$.

TAK-242 (Resatorvid), a novel cyclohexene derivative, is a specific TLR4 signaling inhibitor that interferes with the interaction between TLR4 and its adaptor molecules[34,35]. TAK-242 is suitable for controlling the inflammatory process and improving intestinal injury in both acute and chronic intestinal inflammation models[36–38]. In the control group, LRRK2 transgenic rats displayed shorter small intestine length. However, TAK-242 rescued the shortened small intestine length in LRRK2 transgenic rats (Fig. 6a, c). HE staining showed that the LP of WT, LRRK2^{R1627P} and LRRK2$^{-/-}$ rats treated with TAK-242, became sparse compared with the control group, which may be related to the suppression of innate immunity by long-term TAK-242 injection (Fig. 6b). After measuring the villus height and crypt depth, TAK-242 reversed the phenotype of reduced villus height and crypt

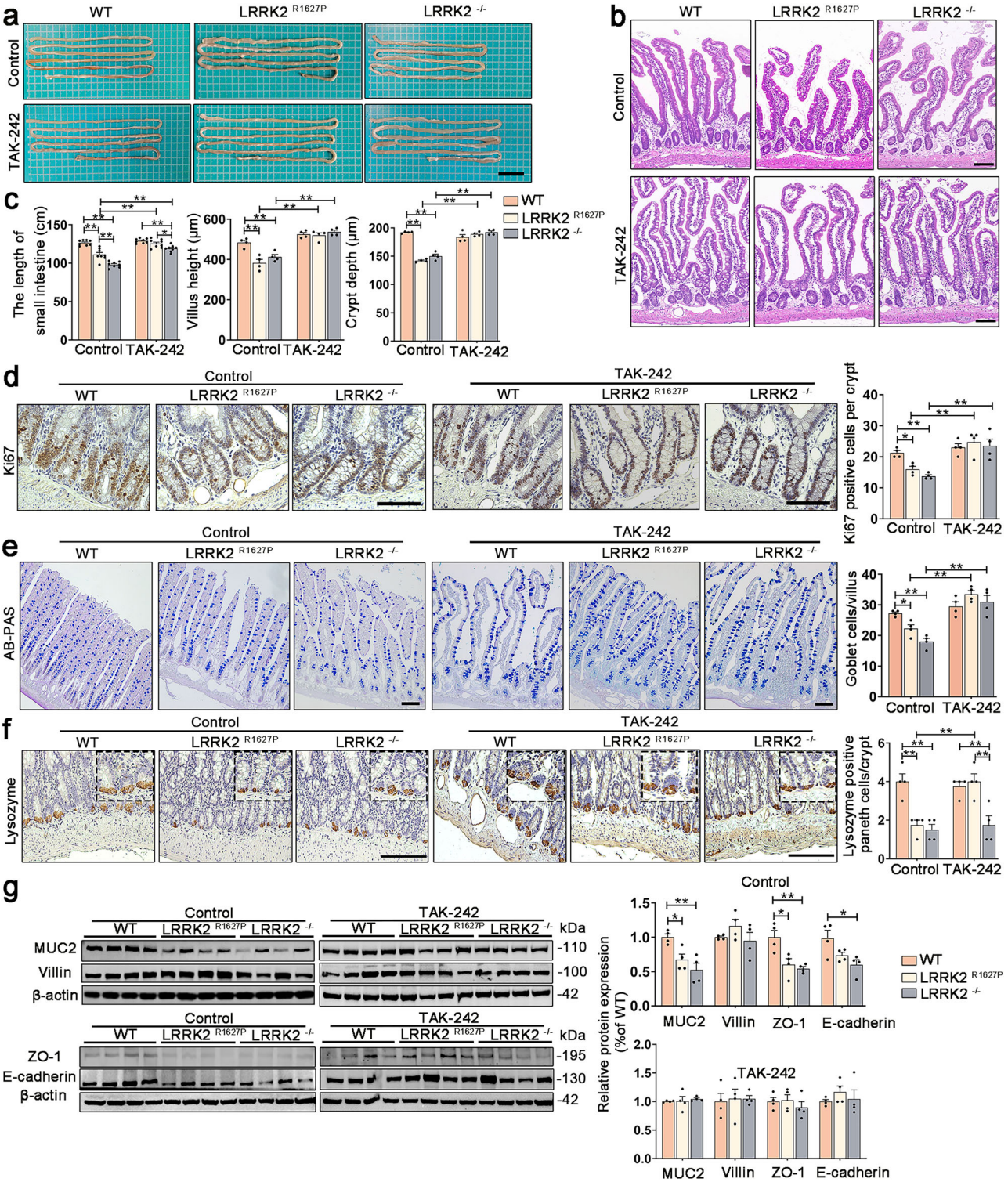

Fig. 6 | Effects of TLR4 inhibitor on IECs proliferation, differentiation and intestinal barrier. a The representative small intestine images in rats treated with saline (control) or TLR4 inhibitor (TAK-242). Scale bar 5 cm, $n = 8$. **b** HE staining images of small intestine in rats treated with saline (control) or TLR4 inhibitor (TAK-242). Scale bar 100 μm, $n = 4$. **c** Measurement of small intestine length ($n = 8$), villus height and crypt depth ($n = 4$) in rats treated with saline (control) or TLR4 inhibitor (TAK-242). Two-way ANOVA was used; interaction $p < 0.0001$. **d** Immunohistochemical staining images of Ki67 in the small intestine, and the quantification of Ki67 positive cells in the crypts (determined based on the number of brown-stained cell nuclei in the crypts). Scale bar 100 μm, $n = 4$. Two-way ANOVA was used; interaction $p < 0.05$. **e** Images and quantification of goblet cells stained with AB-PAS in the small intestine. Scale bar 100 μm, $n = 4$. Two-way ANOVA was used; interaction $p < 0.01$. **f** Images and quantification of immunohistochemical staining for lysozyme in the crypt. Scale bar 100 μm, $n = 4$. Two-way ANOVA was used; interaction $p < 0.01$. **g** Western blot analysis for MUC2, Villin, ZO-1 and E-cadherin protein levels in the small intestine of WT, LRRK2^{R1627P} and LRRK2$^{-/-}$ rats treated with saline (control) or TLR4 inhibitor (TAK-242), $n = 4$. One-way ANOVA was used. Data are presented as mean ± SEM, $^{*}p < 0.05$, $^{**}p < 0.01$.

depth in LRRK2 transgenic rats (Fig. 6c). Furthermore, TAK-242 rescued the expression of Ki67 and the differentiation of goblet cells in LRRK2 transgenic rats (Fig. 6d, e). Notably, TAK-242 did not show a satisfactory recovery in the number of lysozyme-positive Paneth cells in the crypts of $LRRK2^{-/-}$ rats (Fig. 6f). The downregulated protein levels of MUC2, ZO-1 and E-cadherin in the LRRK2 transgenic rats of control group were significantly upregulated after TAK-242 treatment (Fig. 6g, Supplementary Fig. S10a). On top of that, TAK-242 treatment lowered the protein levels of TLR4, MyD88, NF-κB and CD68 in the small intestine of LRRK2 transgenic rats to the same level as those of WT rats as depicted in Fig. 7a, b and Supplementary Fig. S10a, b. Immunofluorescence staining results revealed a significant suppression in the expression levels of M1 macrophage marker CD68, its released pro-inflammatory mediators IL-6 and iNOS, as well as the co-localization of p-α-Syn and M1 macrophage in the LP of WT, $LRRK2^{R1627P}$ and $LRRK2^{-/-}$ rats following TAK-242 injection (Fig. 7c). The RNA-seq results presented in the bubble plot indicated that TAK-242 significantly influenced the expression of genes associated with intestinal immunity and stimulation (Fig. 7d). The heatmap further illustrated that, in comparison with the Control WT (ConWT) group, the immune system process-related DEGs that were upregulated in the Control $LRRK2^{R1627P}$ (ConRP) group were significantly downregulated in the TAK-242 treated $LRRK2^{R1627P}$ (TAKRP) group. The DEGs that were downregulated in the ConRP group were upregulated in the TAKRP group (Fig. 7e). A similar trend was observed in $LRRK2^{-/-}$ rats (Supplementary Fig. S10c, d). In conclusion, the TLR4 inhibitor effectively attenuated the aberrant activation of the innate immune response, pathogenic α-Syn expression and ameliorated intestinal pathology in both $LRRK2^{R1627P}$ and $LRRK2^{-/-}$ rats.

Effects of TLR4 inhibitor on gut microbiota of $LRRK2^{R1627P}$ rats

To investigate the impact of TAK-242 on the gut microbiota environment, we performed 16S rRNA sequencing on the proximal small intestine contents of rats. As the number of reads increased, the rarefaction curves based on the Sobs index and Shannon index gradually smoothed, indicating sufficient sequencing depth. The Pan/Core analysis curve also flattened, suggesting an adequate number of sequenced samples (Supplementary Fig. S11a). Alpha diversity analysis was conducted at the OTU level. Compared with the ConWT group, several indexes positively correlated with alpha diversity, including the Shannon, Ace, Chao, and Sobs index, were significantly decreased in the ConRP group. Conversely, the Simpson index, which is negatively correlated with alpha diversity, was significantly increased in the ConRP group. These findings indicate that microbiota community richness and diversity in the small intestinal contents of ConRP rats were markedly lower than those observed in the ConWT group. Notably, TAK-242 treatment markedly enhanced microbial richness and diversity in $LRRK2^{R1627P}$ rats (Fig. 8a), and similar effects were observed in $LRRK2^{-/-}$ rats (Supplementary Fig. S12a). The microbial dysbiosis index (MDI) is employed to assess the degree of microbial ecological imbalance, with higher values indicating greater dysbiosis. TAK-242 significantly reduced the MDI in LRRK2 transgenic rats, effectively modulating the dysbiotic microbiota (Fig. 8b, Supplementary Fig. S12b).

Subsequently, we aimed to characterize the microbial composition of the small intestinal contents, which revealed distinct community structures across various taxonomic levels. Through the visualization of a Circos plot, the analysis of microbial composition at the phylum level reveals Firmicutes (79%) and Actinobacteria (21%) as the dominant phyla in the ConWT group. However, the microbiota of ConRP and Control $LRRK2^{-/-}$ (ConKO) rats was predominantly composed of Firmicutes, comprising 99% of the total. TAK-242 had shown the capability to reduce the abundance of Firmicutes to 90% and increase the abundance of Actinobacteriota to 9% in $LRRK2^{R1627P}$ rats. This trend was observed in $LRRK2^{-/-}$ rats as well (Supplementary Fig. S11b). The improvement in species richness and composition due to TAK-242 was also evident at the family level (Supplementary Fig. S11c). At the genus level, the effects of TAK-242 on the top 20 most abundant species were clearly illustrated through bar plots and heatmaps featuring distinct color blocks. In both ConRP and ConKO rats, *Lactobacillus* was identified as the predominant genus (Fig. 8c, d, Supplementary Fig. S12c, d). TAK-242 effectively suppressed the *Lactobacillus* overgrowth induced by the $LRRK2^{R1627P}$ mutation while increasing the abundance of genera such as *Romboutsia*, *Corynebacterium*, *Streptococcus*, *Staphylococcus*, *Turicibacter*, *Rothia*, *Jeotgalicoccus*, *Lactococcus*, *Globicatella*, and *Aerococcus*, restoring their levels to more comparable to that of ConWT rats (Fig. 8c, d). We also conducted LEfSe analysis to identify genus with significant differences in abundance, with results quantitatively presented using LDA score bar charts and cladograms. In the top 10 characteristic genera of TAKRP group, *Romboutsia*, *Turicibacter*, *Corynebacterium*, *Staphylococcus*, *Aerococcus* and *Jeotgalicoccus* were also dominant genera in the ConWT group (Fig. 8e). Statistical analysis of the top five genera among the three groups revealed that TAK-242 significantly reduced the increase in *Lactobacillus*, while also significantly enhancing the decrease in *Romboutsia*, *Corynebacterium*, *Staphylococcus* and *Turicibacter* caused by the mutation (Fig. 8f).

After predicting the potential phenotype of bacteria in the ConWT, ConRP, and TAKRP groups by BugBase, it was observed that the relative abundance of Gram negative and aerobic bacteria significantly increased in the ConRP group compared with the ConWT group. TAK-242 treatment reduced the elevated levels of Gram negative and aerobic bacteria in $LRRK2^{R1627P}$ rats (Fig. 8g, h). By combining PICRUSt2 with the KEGG database to predict the biological functions of the microbiota, we analyzed the differences in functional pathways at KEGG levels 1 and 2 among the groups. KEGG level 1 predictions showed that the biological functions of the microbiota in the TAKRP group were more similar to those of ConWT. According to the KEGG level 2 results, predictions related to metabolism, such as amino acid, energy, vitamins and xenobiotics metabolism, were significantly decreased, while disease-related predictions, cancer and nervous system diseases, were notably increased in the $LRRK2^{R1627P}$ rats. TAK-242 effectively restored the dysregulated microbiota biological functions caused by the $LRRK2^{R1627P}$ mutation (Fig. 8i, j). The beneficial modulation of microbial structure and function by TAK-242 was also observed in $LRRK2^{-/-}$ rats (Supplementary Fig. S12e–j). In summary, the TLR4 inhibitor could influence the composition characteristics of the gut microbiota, increasing the diversity and richness of the microbiota in LRRK2 transgenic rats.

Discussion

This study reveals that the $LRRK2^{R1627P}$ (human $LRRK2^{R1628P}$) progressively disrupts intestinal homeostasis in rats across their lifespan, manifesting as impaired epithelial proliferation and differentiation, compromised barrier integrity, p-α-Syn pathology, and microbial dysbiosis. These changes are driven by TLR4/NF-κB signaling pathway and macrophage dysfunction. Treatment with TAK-242, a selective TLR4 inhibitor, resulted in a significant improvement in the disrupted intestinal homeostasis of $LRRK2^{R1627P}$ rats. In addition, our observations indicate that $LRRK2^{R1627P}$ rats exhibit an exaggerated inflammatory response to LPS stimulation (Fig. 9). These findings have provided a strong longitudinal perspective on how $LRRK2^{R1627P}$ interact with aging and toxin exposure to promote chronic inflammation and p-α-Syn pathology in the gut, suggesting TLR4/NF-κB pathway modulation or microbiota intervention as potential preventive strategies for LRRK2-related PD.

Consistent with our previous findings in rat brains[29], the $LRRK2^{R1627P}$ represented a "loss-of-function" mutation (decreased total LRRK2 and phosphorylated Rab10 level) in the gut. This observation aligns with the expression trend of LRRK2 and Rab10 in the colons of sporadic PD patients[39]. However, in the colon of mice, $LRRK2^{R1628P}$ represented a "gain-of-function" mutation (unchanged total LRRK2 protein levels but increased phosphorylated Rab10 level) in mouse colon[27]. Further validation in intestinal tissues of humans carrying the $LRRK2^{R1628P}$ mutation is warranted to elucidate the species-specific of this mutation and its potential pathogenic mechanisms. The relationship between LRRK2 protein, its kinase activity, and intestinal inflammation remains inadequately understood. Studies have shown that the $LRRK2^{G2019S}$ increases its kinase activity, accelerating the

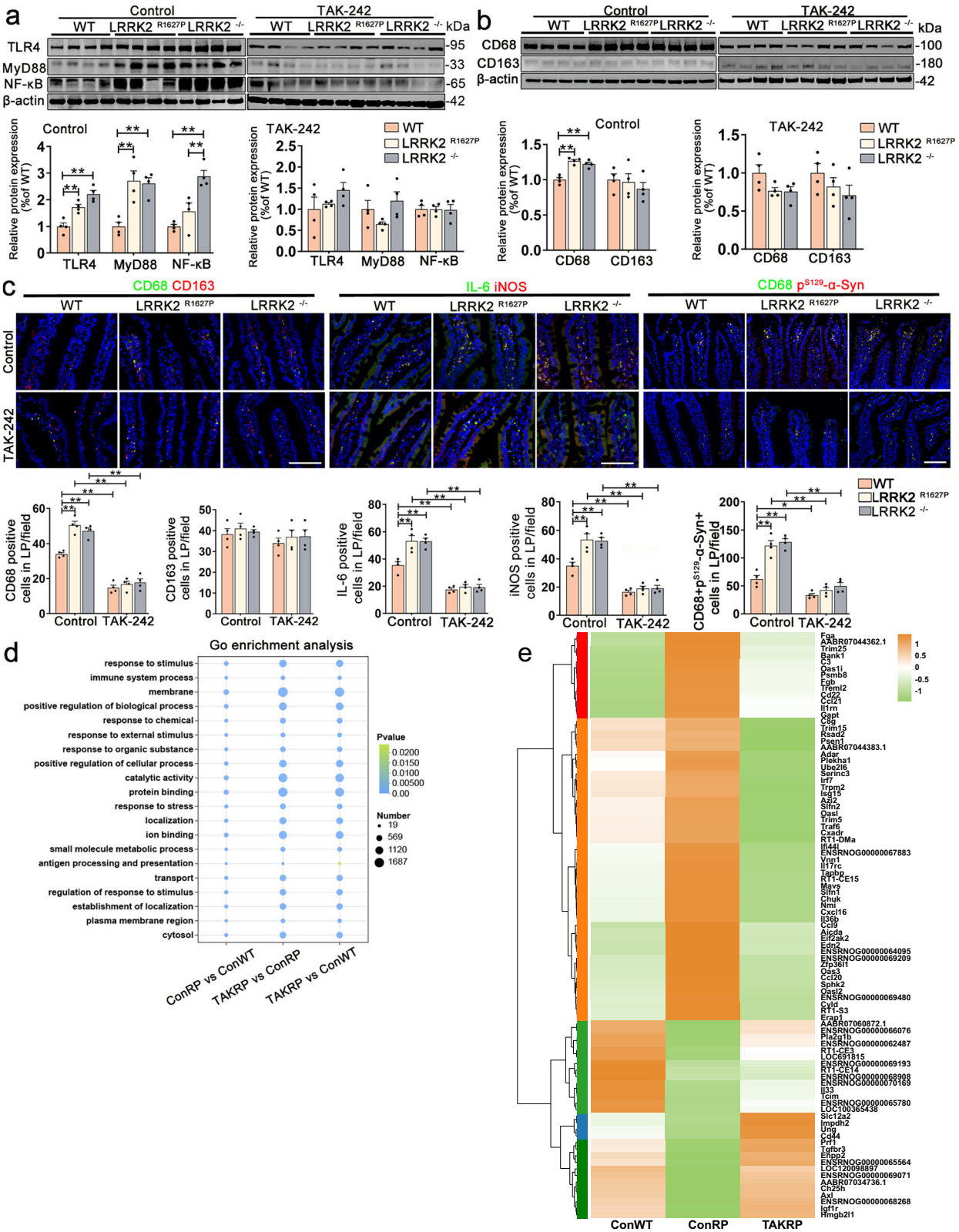

Fig. 7 | Effects of TLR4 inhibitor on intestinal innate immunity and pathological α-Syn expression. a, **b** Western blot analysis for TLR4, MyD88, NF-κB, CD68 and CD163 protein levels in the small intestine of WT, LRRK2^{R1627P} and LRRK2$^{-/-}$ rats treated with saline (control) or TLR4 inhibitor (TAK-242), $n = 4$. One-way ANOVA was used. **c** Immunofluorescence staining images and quantification of CD68/IL-6 (green) and CD163/iNOS/p^{S129}-α-Syn (red) positive cells in the small intestinal LP of rats treated with saline (control) or TLR4 inhibitor (TAK-242). Nuclei were stained with DAPI (blue). Scale bar 100 μm, $n = 4$. Two-way ANOVA was used; for CD68/IL-6/iNOS analysis interaction $p < 0.01$; for CD163 analysis interaction $p > 0.05$; for p^{S129}-α-Syn analysis interaction $p < 0.001$. **d** GO enrichment analysis for DEGs in ConRP vs ConWT, TAKRP vs ConRP, TAKRP vs ConWT, $n = 3$. **e** Heatmap of DEGs from ConWT, ConRP and TAKRP group, $n = 3$. Data are presented as mean ± SEM, $^{*}p < 0.05$, $^{**}p < 0.01$.

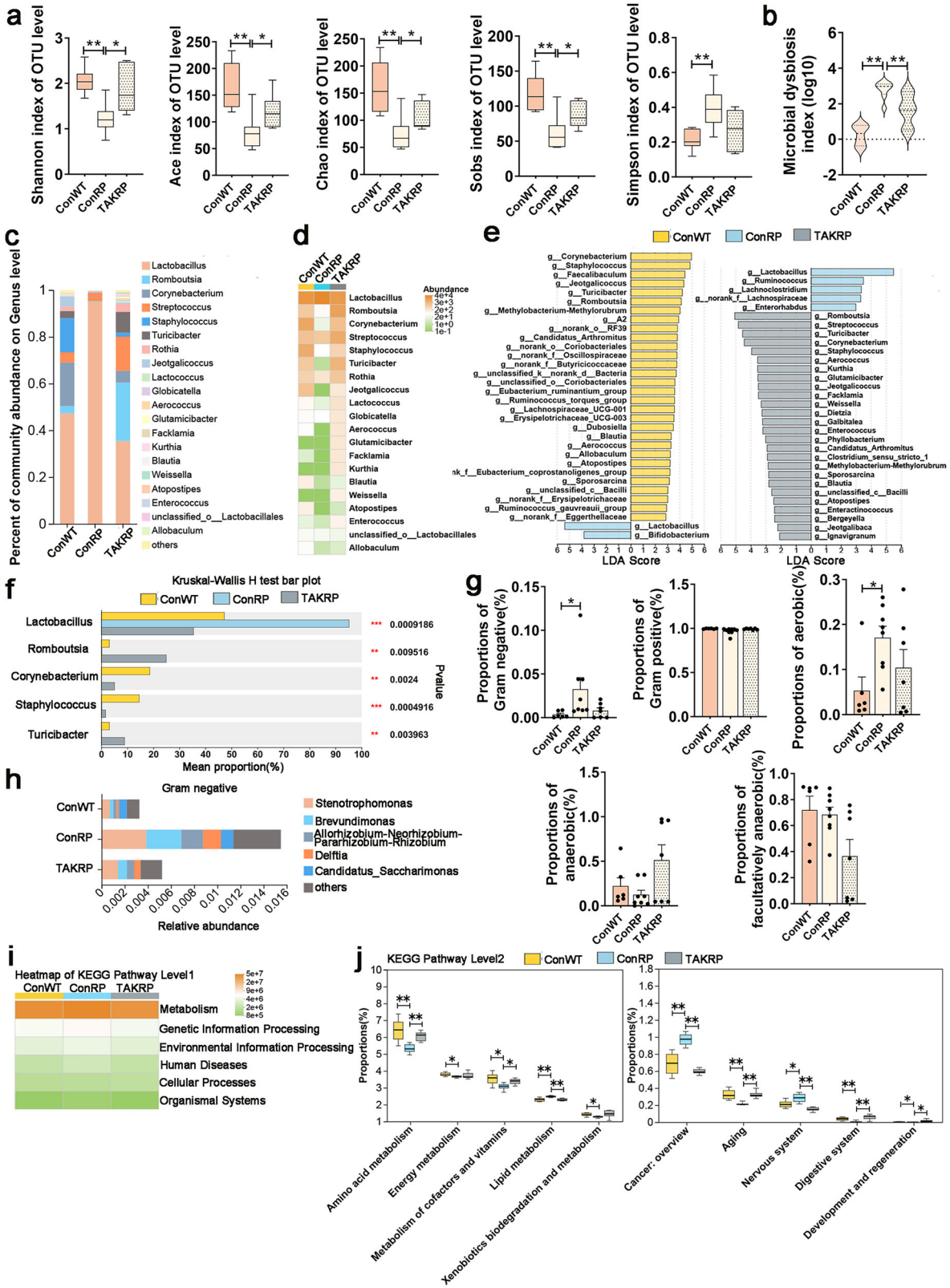

Fig. 8 | Effects of TLR4 inhibitor on intestinal microbial community composition and function in LRRK2^{R1627P} rats. a Alpha-diversity was determined using Shannon index, Ace index, Chao index, Sobs index, and Simpson index based on OTU level. **b** Comparison of the microbial dysbiosis index in ConWT, ConRP and TAKRP group. **c** Bar plot of the top 20 most abundant species at genus level. **d** Heatmap to visualize the top 20 most abundant species at genus level. **e** LEfSe analysis of characteristic microbial composition in three groups. LDA score threshold > 2.0. **f** Species difference test of top 5 most abundant species at genus level. **g** Gut microbiota phenotypes based on BugBase predictive analysis, including Gram negative, Gram positive, aerobic, anaerobic, facultatively anaerobic. Non-parametric test was used. **h** Species composition of Gram negative phenotypes. **i**, **j** KEGG level1 and level2 annotations by PICRUSt2-predicted based on 16S rRNA gene sequencing data of the three groups. $n = 6$ in ConWT, $n = 8$ in ConRP, $n = 7$ in TAKRP. $^{*}p < 0.05$, $^{**}p < 0.01$.

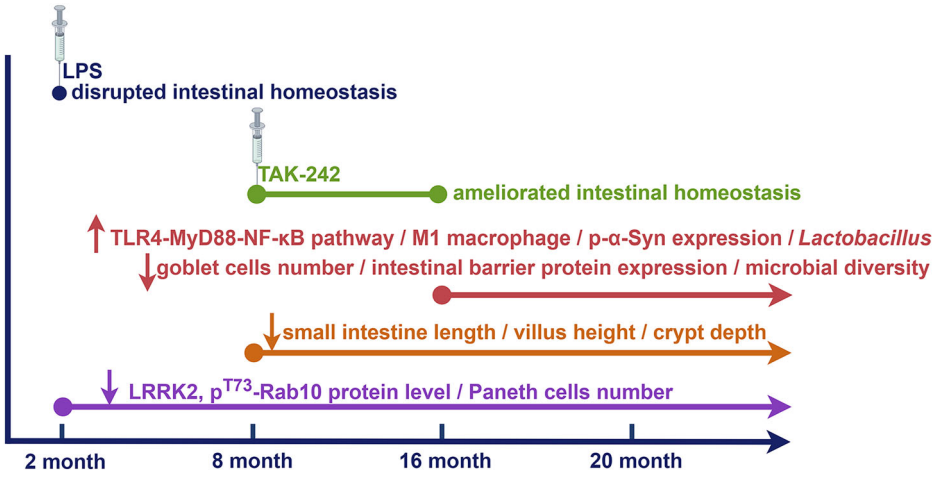

Fig. 9 | Dynamic changes of small intestinal homeostasis in LRRK2^{R1627P} rats from young to old. LRRK2^{R1627P} mutation significantly reduced intestianl endogenous total LRRK2, pT73-Rab10 protein level and the number of Paneth cells. Compared with age-macthed WT rats, LRRK2^{R1627P} rats showed shorter small intestine length, villus height, and crypt depth (from 8 months old); a significant decrease in the number of goblet cells, expression of barrier proteins, and microbial community diversity (from 16 months old); and a marked increase in the TLR4/MyD88/NF-κB signaling pathway, the number of M1 macrophages, the expression of p^{S129}-α-Syn, and the abundance of *Lactobacillus* (from 16 months old). Long-term administration of the TLR4 inhibitor TAK-242 effectively ameliorated the imbalance in intestinal homeostasis of LRRK2^{R1627P} rats.

progression of DSS-induced colitis[16]. In contrast, the LRRK2^{M2397T} decreases LRRK2 protein levels without altering its kinase activity, resulting in abnormal Paneth cell phenotypes[40–42]. Conflicting reports exist regarding whether LRRK2$^{-/-}$ ameliorates or exacerbates intestinal inflammation[22,41]. These findings suggest that LRRK2 plays a dual regulatory role in maintaining intestinal homeostasis, requiring its protein levels and kinase activity to be tightly regulated within a precise physiological range.

Alone, LRRK2 mutations do not induce spontaneous PD in animals. In young LRRK2^{R1627P} transgenic rats, we only observed reduced lysozyme-positive Paneth cells, consistent with Qin Zhang et al.'s findings linking this defect to impaired LRRK2-Rab2a signaling and mistrafficking of lysozyme[43]. However, aging triggered PD-like features in the gut of LRRK2^{R1627P} rats, including progressive intestinal inflammation and p-α-Syn deposition, suggesting their potential utility in studying the contribution of the gut-brain axis to PD pathogenesis. We found that age-dependent increases in p-α-Syn in the small intestine were predominantly localized to pro-inflammatory macrophages, rather than neurons in the myenteric plexus. Pro-inflammatory macrophages can promote the pathological modification of α-Syn through NF-κB signaling[44,45], and age-related phagocytic and clearance dysfunction exacerbates α-Syn accumulation[46]. Meanwhile, α-Syn can act as a TLR4 ligand and amplify the pro-inflammatory phenotype of macrophages[47–50]. Therefore, genetic and aging factors can establish a self-reinforcing vicious cycle between chronic inflammation and pathological α-Syn aggregation. This process may facilitate pathological α-Syn migration via macrophages from the gut to blood, and brain, triggering broader pathological responses that could lead to the onset and progression of PD. Notably, the penetrance of LRRK2^{G2019S}, the most common LRRK2 mutation in PD, has been reported to increase with advancing age[51]. Although lifespan of LRRK2^{R1627P} rats precluded long-term observation, this mutation's dual effects that accelerating dopaminergic neuron senescence[29] and promoting chronic intestinal inflammation with pathological α-Syn aggregation in responses to senescence signals, should be regarded as a potential early warning marker driving PD pathogenesis.

Although LRRK2^{R1627P} rats exhibited PD -related pathological phenotypes in the gut during aging, we found they did not develop typical PD[29]. This aligns with the low penetrance of PD observed in LRRK2^{R1628P} carriers[52], suggesting that the genetic susceptibility and aging is insufficient to fully drive PD pathogenesis. Previous studies indicate that exogenous stimuli to induce intestinal injury can accelerate PD progression in LRRK2 models[16,27,53]. To further explore this, we assessed the effects of LPS on LRRK2^{R1627P} rats. A single 6 h LPS exposure induced severe damage and elevated p-α-Syn level in the gut of LRRK2^{R1627P} rats without acute brain abnormalities (data not shown). However, acute intestinal inflammation could still lead to delayed, cumulative central nervous system (CNS) inflammation, warranting longer-term observation to determine whether the LRRK2^{R1627P} increases neurodegeneration risk. Supporting this, our prior work showed that repeated low-dose LPS exposure in aged LRRK2^{R1627P} rats triggered neuroinflammation and α-Syn pathology in the substantia nigra[29]. Notably, in LRRK2^{G2019S} mice with chronic colitis, only CNS inflammation infiltration was observed. TH^{+} cells loss and motor deficits required additional stereotaxic α-Syn injection into the substantia nigra[53]. These underscore the potential of LRRK2^{R1627P} model for PD research. Optimizing LPS protocols (dose, duration) or incorporating additional stimuli may better replicate PD pathology and elucidate mechanisms of PD conversion in LRRK2 carriers.

Notably, multiplex immunofluorescence staining revealed that the expression of TLR4 and p-α-Syn was not localized to neurons in the muscular layer, but was distributed in the M1 macrophages (Supplementary Figs. S7, S8). This finding contrasts with the classical view that abnormal α-Syn expression typically originates in enteric neurons and may retrogradely propagate via the vagus nerve. In the context of the LRRK2^{R1627P}, aberrant p-α-Syn expression originates from active macrophage driven by TLR4. Thus, our findings suggest that LRRK2-mediated gut-brain axis communication is closely associated with immune circulation pathway. Elucidating the specific role of this pathway in the propagation of PD pathology will be an important direction for future research.

In summary, combined with our prior work[29], the LRRK2^{R1627P} rats exhibited chronic intestinal inflammation, p-α-Syn dysregulation, and central neuroinflammatory driven by the synergistic amplification of genetic risk, aging and toxin exposure, which recapitulated the progressive peripheral-to-central pathological cascade of PD. This model provides compelling evidence for deciphering the "multiple-hit" pathogenesis of PD, bridging gaps between traditional single-factor models and the complex pathophysiological processes of human PD, and offering a robust platform for mechanistic and therapeutic exploration.

Studies have revealed a close relationship between LRRK2 and TLR4/NF-κB. As a potential DUSP-mediated hub in TLR4 signaling[54], LRRK2 can also negatively regulate NF-κB p50 DNA-binding and transcriptional activity[55]. We found that the TLR4/NF-κB-driven macrophage inflammatory response contributes to intestinal homeostasis disruption in LRRK2^{R1627P} rats (reduced LRRK2 kinase activity). Notably, analogous results have also been observed in LRRK2^{G2019S} and LRRK2^{R1441C} mice (increased kinase activity)[16,22]. Additionally, the precise relationship between TLR4-mediated macrophage inflammation and LRRK2 kinase activity remains inconclusive in vitro[56–60]. These reveal the complex regulatory role of LRRK2 in inflammation, where any perturbation of its kinase activity may compromise intestinal homeostasis via TLR4/NF-κB signaling. Given the aberrant TLR4 activation in the gut of PD patients and animal models[61], along with TAK-242's amelioration of intestinal inflammation and p-α-Syn aggregation in our study, it is hypothesized

that targeting the TLR4 signaling in the gut is crucial for halting the insidious progression of PD.

In addition, we observed severe gut microbiota dysbiosis in LRRK2^{R1627P} rats, characterized by *Lactobacillus* as the dominant species, alongside a significant decrease in other beneficial bacteria, including short-chain fatty acid-producing *Romboutsia* and *Blautia*[62,63], LPS-negative correlated *Turicibacter*[64], and TLR4/NF-κB signaling pathway-negative correlated *Aerococcus*[65]. While *Lactobacillus* is typically probiotic, its enrichment in LRRK2^{R1627P} rats, mirroring findings in PD and CD patients[66–68], suggests a complex role in gut homeostasis. This overgrowth may represent a compensatory response to homeostatic imbalance or actively disrupt homeostasis by altering gut pH through lactic acid production, inhibiting symbiotic bacteria, and exacerbating dysbiosis[69]. Excessive *Lactobacillus* and its metabolic products could also burden the gut barrier and immune system[70], perpetuating chronic inflammation. In PD patients, *Lactobacillus* enrichment correlates with worsened motor symptoms[71,72], interfered levodopa absorption[73], reduced neuroprotective Ghrelin[74], and potential modulation of α-Syn secretion[75,76]. Determining whether *Lactobacillus* enrichment is compensatory or causative is critical for elucidating LRRK2-related intestinal pathologic mechanisms and developing therapies targeting gut inflammation and α-Syn propagation.

Previous studies demonstrate that inhibiting gut inflammation or modulating gut microbiota in LRRK2 models alleviates dopaminergic neuron loss and motor deficits[16,27], underscoring intestinal homeostasis as a therapeutic target for LRRK2-linked PD. Interventions such as TLR4 inhibition, anti-TNF-α therapy, or microbiota transplantation may restore gut balance, block α-Syn propagation to the CNS, and lower neurodegeneration risk. Our findings emphasize the pivotal role of LRRK2 in gut health, where its dysfunction may serve as an upstream event in LRRK2-associated PD. Targeting intestinal homeostasis offers a feasible approach to preserving the integrity of the gut-brain axis and intervening in the early pathological progression of PD.

Through systematic investigation of LRRK2^{R1627P} rats, we showed the interplay between genetic susceptibility and environmental triggers (age and toxin) in driving early pathological features of PD. This model not only provides new insights into the impact of LRRK2 mutation heterogeneity (such as "loss-of-function" variant) on intestinal homeostasis but also recapitulates the progressive pathological evolution of PD from the gut to the brain. Finally, we emphasize that early intervention strategies aimed at protecting gut-brain axis integrity through modulation of intestinal immune inflammation or microbial composition may be crucial for blocking the conversion of LRRK2-related PD or delaying disease progression.

Methods

Animal experiments

All experiments involving rats were approved by the Animal Care and Use Committee of the Capital Medical University and were conducted in compliance with all relevant ethical regulations for animal testing and research. All experiments involving rats comply with the Animal Research.

LRRK2^{R1627P} knock-in and LRRK2 knock-out rats were generated as described previously[29]. All procedures were approved by the Animal Care and Use Committee of the Capital Medical University. Rats were kept on a 12 h light/12 h dark cycle, at 20–22 °C, with ad libitum access to food and water. The experimental design for the animal studies is shown in Supplementary Fig. S1. For comparing intestinal homeostasis in animals at different age stages (2, 8, 16, and 20–22 months), 15 animals were used in each group.

TAK-242 administration: TLR4 inhibitor TAK-242 was purchased from MedChemExpress (Monmouth Junction, NJ, USA), HY-11109. 8-month-old female WT, LRRK2^{R1627P} and LRRK2$^{-/-}$ rats were intraperitoneally injected with TAK-242 (3 mg kg^{-1}; TAK-242 dissolved in sterile saline containing 1% DMSO) daily. After 2 months, we observed alopecia in most of the animals. Then the treatment regimen was modified to intraperitoneal injection every other day (3 mg kg^{-1}), and the rats were sacrificed after 6 months of treatment. The control rats were injected with the same dose of sterile saline containing 1% DMSO. 12 rats were used in each group.

LPS administration: LPS (*Escherichia coli* O55:B5, L2880) was purchased from Sigma-Aldrich (Saint Louis, MO, USA). 2-month-old female WT, LRRK2^{R1627P} and LRRK2$^{-/-}$ rats were intraperitoneally injected with LPS (5 mg kg^{-1}; LPS dissolved in sterile saline), 8 rats in each group. The rats were sacrificed 6 h later. The control rats were injected with the same dose of sterile saline. 8 rats were used in each group.

Histomorphological analysis

Quickly removed and measured the full length of the small intestine from rats. Collected tissue samples, approximately 20 cm to root of the stomach as indicated in Fig. 2b, for all experiments. Following fixation in 4% paraformaldehyde solution for 48 h, tissues were embedded in paraffin and sections were made at a thickness of 4 μm. Standardized intestinal tissues hematoxylin-eosin (HE) staining were performed according to the HE staining kit (Servicebio, G1005). Villus height and crypt depth were measured by Case Viewer software. The villus height was measured from the apex of villus to the villus-crypt junction; the crypt depth was measured from the villus-crypt junction to the crypt base. For each animal, four fields of view were randomly selected for measurement.

Reverse transcription-quantitative polymerase chain reaction (RT-qPCR)

Total RNA was extracted from small intestine by Trizol (Thermo Fisher Scientific, 15596018CN), and the concentration of RNA was measured by NanoDrop 2000 spectrophotometer. Reverse transcription reaction was performed according to the instructions of the Promega reverse transcription kit (A5003). LightCycler® 480 SYBR Green I Master (Roche, 04707516001) to quantify gene expression and GAPDH was used as an internal standard to normalize LRRK2 mRNA levels. The primer sequences used in this experiment are as follows: LRRK2 forward 5'-CGAAGGAGA GGAAGTGGCTG-3' and reverse 5'-GCTGGGATGGTGGAGATGAC-3'; GAPDH forward 5'-TGGCCTTCCGTGTTCCTACC-3' and reverse 5'-C GCCTGCTTCACCACCTTCT-3'.

Western blot analysis

Jejunal tissues were homogenized using a cryogenic tissue grinder at 70 Hz in RIPA lysis buffer supplemented with cOmplete protease inhibitor and PhosSTOP phosphatase inhibitor (Roche). The Qubit protein assay kit (Thermo Fisher Scientific, Q33212) was used to determine the total protein concentration of the supernatant. Protein was separated by electrophoresis on sodium dodecyl sulfate-polyacrylamide gel using Mini Trans-Blot system (Bio-Rad) and then transferred to polyvinylidene fluoride membranes. Membranes were blocked with 5% bovine serum albumin (BSA) for 2 h at room temperature, followed by incubation of primary antibodies overnight at 4 °C. Antibody information: LRRK2 (Abcam, ab133474, 1:500), phosphorylated S935 LRRK2 (ABclonal, AP1154, 1:500), Rab8a (Santa Cruz Biotechnology, sc-81909, 1:200), phosphorylated T72 Rab8a (Abcam, ab230260, 1:500), Rab2 (Santa Cruz Biotechnology, sc-133059, 1:200), Rab5a (Affinity Biosciences, AF4073, 1:500), Rab10 (Affinity Biosciences, #DF7582, 1:500), phosphorylated T73 Rab10 (Abcam, ab241060, 1:500), MUC2 (ABclonal, A4767, 1:1000), Villin (Servicebio, GB121209, 1:1000), ZO-1 (ABclonal, A11417, 1:500), E-cadherin (Cell Signaling Technology, 14472, 1:1000), TLR4 (Servicebio, GB11519, 1:1000), MyD88 (Servicebio, GB111554-100, 11000), NF-κB (Servicebio, GB11997-100, 1:1000), CD68 (Santa Cruz Biotechnology, sc-20060, 1:200), CD163 (Servicebio, GB11340, 1:1000), β-actin (Servicebio, GB15001, 1:2000), GAPDH (Servicebio, GB15002, 1:3000), Lamin A/C (Servicebio, GB11407, 1:1000). The membranes were visualized with VILBER system and protein bands were quantified using ImageJ software.

Immunohistochemical staining

Small intestine paraffin sections were dewaxed and rehydrated by xylene and ethanol. Sections were placed in boiled sodium citrate buffer for 20 min

to antigen repair. Subsequently, sections were incubated with 3% hydrogen peroxide for 25 min to eliminate endogenous peroxidase and blocked with 5% BSA for 1 h to minimize non-specific staining. Sections were then incubated with primary antibodies overnight at 4 °C. Antibody information: Ki67 (Servicebio, GB111141, 1:500), Lysozyme (Servicebio, GB11345, 1:500), Cleaved caspase 3 (Servicebio, GB11532, 1:500). The target protein was visualized with SABC staining kit (BOSTER, SA1028) and diaminobenzidine (BOSTER, AR1022). Nuclei were stained with hematoxylin. For each animal, four fields of view were randomly selected for measurement.

Immunofluorescence staining

Small intestine paraffin sections were dewaxed, rehydrated, antigen repair, blocked and then incubated with primary antibodies overnight at 4 °C. Antibody information: LRRK2 (Abcam, ab133474, 1:200), βIII-Tubulin (Servicebio, GB15139, 1:500), CD68 (Santa Cruz Biotechnology, sc-20060, 1:100), CD163 (Servicebio, GB11340-1, 1:200), iNOS (Affinity Biosciences, AF0199, 1:200), IL-6 (Cell Signaling Technology, D5W4V, 1;200), p^{S129}-α-Syn (Cell Signaling Technology, 23706S, 1:200). Sections were subsequently incubated with fluorescein isothiocyanate (FITC) - or phycoerythrin (PE) - conjugated secondary antibodies for 1 h at room temperature. Nuclei were stained with DAPI. For each animal, four fields of view were randomly selected for measurement.

Alcian blue and periodic acid-schiff (AB-PAS) staining

AB-PAS staining was performed according to the AB-PAS staining kit (Servicebio, G1049). Briefly, paraffin sections of small intestine were stained with alcian blue solution for 8 min, periodic acid solution for 15 min and schiff solution for 30 min in the dark. Finally, the sections were dehydrated and sealed with neutral gum. For each animal, four fields of view were randomly selected for measurement.

Flow cytometry

The rat small intestines were washed with cold PBS and cut into 1 cm pieces. Tissue pieces were incubated in 5 mM EDTA-HBSS solution for 30 min at 37 °C. Tissue pieces were thoroughly washed in warm HBSS solution to inactivate EDTA. Following this, tissues were minced finely and incubated in fresh medium containing 0.2% collagenase II (Gibco) for 40 min at 37 °C. The digestion was terminated by adding an equal volume of medium containing 20% fetal bovine serum and the supernatant was collected through cell strainers of 70 μm and 40 μm. Cells were incubated with anti-CD11b (FITC-conjugated, BD Pharmingen, 554982, 1:100), CD68 (APC-conjugated, Novus, SPM130, 1:100), CD163 (Percp-conjugated, Novus, NBP2 39099, 1:100) antibodies. Stained cells were detected with BD FACSCalibur™ Flow Cytometer and analyzed by FlowJo software.

Transmission electron microscopy (TEM)

Small intestines (1 mm^3) were fixed in 2.5% glutaraldehyde and post-fixed with 1% osmium tetroxide and 1% uranyl acetate. Small intestines were dehydrated through graded alcohols and embedded in resin. The prepared ultrathin sections were placed on copper grids, stained with uranyl acetate and lead citrate, then observed on a JEM-1400 plus TEM at 120 kV. For each animal, four fields of view were randomly selected for measurement.

Tyramide signal amplification (TSA) multiple immunofluorescence staining

Multiplex immunofluorescence staining kit (G1236) was purchased from Servicebio (Wuhan, China). The first antibody: anti-CD68 (Santa Cruz Biotechnology, sc-20060, 1:500) was added to the paraffin sections of the jejunum after dewaxing, hydration, antigen retrieval, and blocking. Sections were washed with TBST and incubated with secondary antibody, followed by the addition of TSA 488 fluorescent dye. Following repeated antigen retrieval, blocking procedures sections were supplemented with a second antibody: anti-βIII-Tubulin (Abcam, ab78078, 1:1000). Sections were washed in TBST and incubated with secondary antibodies followed by the addition of TSA 555 fluorescent dye. After repeat antigen retrieval and blocking procedures, sections were incubated with a third antibody: anti-p^{S129}-α-Syn (Cell Signaling Technology, 23706S, 1:1000) or anti-TLR4 (Servicebio, GB15186, 1:1000). Sections were washed in TBST and incubated with secondary antibodies, and then the TSA 647 fluorescent dye was added. Slides were finally mounted using anti-fluorescent quench mounting medium containing DAPI.

16S ribosomal RNA (16S rRNA) microbiome sequence

After euthanizing the rats, the entire intestine was carefully extracted using a sterile scalpel. The exterior surface of the intestine was rinsed with cold PBS, and a proximal small intestine segment ~10 cm in length was excised. One end of the intestine was secured, and the intestinal contents were gently extruded into a sterile EP tube using sterile forceps. The sample was flash-frozen in liquid nitrogen and stored at −80 °C until further processing. DNA extraction for fecal genomic DNA and 16S rRNA amplification were provide by Majorbio Bio-Pharm Technology Co., Ltd. (Shanghai, China). Total bacterial genomic DNA was extracted using the FastPure Stool DNA Isolation Kit (MJYH, Shanghai, China). The integrity of the extracted DNA was assessed using 1% agarose gel electrophoresis. DNA concentration and purity were measured with a NanoDrop® ND-2000 spectrophotometer (Thermo Fisher Scientific Inc., USA). PCR amplification of the V3-V4 variable regions of the 16S rRNA gene was performed using primers 338F (5'-ACTCCTACGGGAGGCAGCAG-3') and 806R (5'-GGACTACH VGGGTWTCTAAT-3'). PCR products were then purified from a 2% agarose gel and quantified using a Synergy HTX microplate reader (Biotek, USA). According to Majorbio Bio-Pharm Technology Co. Ltd. protocols, the purified amplicons were pooled in equimolar amounts and paired-end sequenced on an Illumina NextSeq 2000 PE300 platform (Illumina, San Diego, USA). The raw paired-end reads were merged based on overlap sequences and filtered for quality control. Following sample differentiation, OTU clustering and taxonomic classification were performed for further analysis. All bioinformatics analysis were performed on the online platform Majorbio Cloud Platform (www.majorbio.com). All obtained raw sequence datasets have been uploaded to the NCBI Sequence Read Archive (SRA) with the accession number PRJNA1236240.

Transcriptome analysis

RNA extraction, purification, reverse transcription, library construction, and sequencing were carried out at Majorbio Bio-Pharm Biotechnology Co., Ltd. (Shanghai, China), following the manufacturer's protocols (Illumina, San Diego, CA). Total RNA was isolated from small intestine tissues using TRIzol® reagent, and RNA quality was assessed with an Agilent 5300 Bioanalyzer, with quantification by an ND-2000 spectrophotometer (NanoDrop Technologies). Only high-quality RNA samples (OD260/280 = 1.8–2.2, OD260/230 ≥ 2.0, RNA integrity number [RIN] ≥6.5, 28S:18S ratio ≥1.0, >1 μg) were used for library construction. Magnetic beads with oligo (dT) bind to the poly (A) tails at the 3' ends of mRNA through A-T base pairing, allowing the isolation of mRNA from total RNA for transcriptomic analysis. The mRNA was then fragmented using a fragmentation buffer. Double-stranded cDNA was synthesized using a SuperScript double-strand cDNA synthesis kit (Invitrogen, CA) with random hexamer primers (Illumina). Following Illumina's library preparation protocols, the resulting cDNA underwent end repair, phosphorylation, and 'A' base addition. Libraries with a target insert size of ~300 bp were selected using 2% low-melting agarose gel, and then amplified by 15 cycles of PCR using Phusion DNA polymerase (NEB). After quantification by Qubit 4.0, paired-end sequencing was performed on the RNA-seq libraries using an Illumina NovaSeq X Plus platform (Illumina, San Diego, CA, USA). The raw sequencing data were subjected to quality control and aligned to the reference genome. Differential gene expression and functional enrichment analyses were subsequently conducted on the Majorbio Cloud Platform (www.majorbio.com). All obtained raw sequence datasets have been uploaded to the NCBI Sequence Read Archive (SRA) with the accession number PRJNA1255462.

Isolation of cytoplasmic and nuclear proteins

Cytoplasmic and nuclear proteins were extracted from jejunum tissue using a commercial kit (Beyotime, China, P0028) according to the manufacturer's instructions. Briefly, minced tissue fragments were homogenized on ice in a pre-mixed buffer (Reagent A:B = 20:1). The homogenate was centrifuged (4 °C, 1500 × *g*, 5 min) to yield an initial cytoplasmic fraction. The pellet was sequentially treated with Reagents A, followed by centrifugation (4 °C, 12,000 × *g*, 5 min) to obtain the total cytoplasmic protein. The final pellet was then resuspended in nuclear extraction reagent and subjected by vortexing. The nuclear fraction was collected by a final centrifugation (4 °C, 12,000 × *g*, 10 min).

Statistical analysis

Graphs are presented as mean ± standard error of the mean (SEM). Statistical analysis was performed using GraphPad Prism 9.5.0 software. The Shapiro-Wilk test was used to assess normality. If the data were normally distributed, differences between two groups were evaluated by Student's *t* test, and differences among three or more groups were assessed using one-way ANOVA or two-way ANOVA followed by Tukey's post hoc test. If the data were not normally distributed, non-parametric test with Dunn's post hoc test was used to evaluate differences between groups. For all analyses, significance was accepted at $p < 0.05$.

Data availability

All raw data generated or analyzed during this study are available from the corresponding author on reasonable request.

Received: 17 May 2025; Accepted: 26 January 2026;
Published online: 07 February 2026

References

1. Clairembault, T. et al. Structural alterations of the intestinal epithelial barrier in Parkinson's disease. *Acta Neuropathol. Commun.* **3**, 12 (2015).
2. Mulak, A., Koszewicz, M., Panek-Jeziorna, M., Koziorowska-Gawron, E. & Budrewicz, S. Fecal Calprotectin as a Marker of the Gut Immune System Activation Is Elevated in Parkinson's Disease. *Front Neurosci.* **13**, 992 (2019).
3. Devos, D. et al. Colonic inflammation in Parkinson's disease. *Neurobiol. Dis.* **50**, 42–48 (2013).
4. Houser, M. C. et al. Stool Immune Profiles Evince Gastrointestinal Inflammation in Parkinson's Disease. *Mov. Disord.* **33**, 793–804 (2018).
5. Schwiertz, A. et al. Fecal markers of intestinal inflammation and intestinal permeability are elevated in Parkinson's disease. *Parkinsonism Relat. Disord.* **50**, 104–107 (2018).
6. Zhang, Z., Liu, Z., Lv, A. & Fan, C. How Toll-like receptors influence Parkinson's disease in the microbiome-gut-brain axis. *Front Immunol.* **14**, 1154626 (2023).
7. Gorecki, A. M., Anyaegbu, C. C. & Anderton, R. S. TLR2 and TLR4 in Parkinson's disease pathogenesis: the environment takes a toll on the gut. *Transl. Neurodegener.* **10**, 47 (2021).
8. Caputi, V. & Giron, M. C. Microbiome-Gut-Brain Axis and Toll-Like Receptors in Parkinson's Disease. *Int J Mol Sci* **19**, 1689 (2018).
9. Kumari, U. & Tan, E. K. LRRK2 in Parkinson's disease: genetic and clinical studies from patients. *FEBS J.* **276**, 6455–6463 (2009).
10. Zimprich, A. et al. Mutations in LRRK2 cause autosomal-dominant parkinsonism with pleomorphic pathology. *Neuron* **44**, 601–607 (2004).
11. Kluss, J. H., Mamais, A. & Cookson, M. R. LRRK2 links genetic and sporadic Parkinson's disease. *Biochem Soc. Trans.* **47**, 651–661 (2019).
12. Barrett, J. C. et al. Genome-wide association defines more than 30 distinct susceptibility loci for Crohn's disease. *Nat. Genet.* **40**, 955–962 (2008).
13. Van Limbergen, J., Wilson, D. C. & Satsangi, J. The genetics of Crohn's disease. *Annu Rev. Genomics Hum. Genet.* **10**, 89–116 (2009).
14. McGovern, D. P., Kugathasan, S. & Cho, J. H. Genetics of Inflammatory Bowel Diseases. *Gastroenterology* **149**, 1163–1176 e1162 (2015).
15. Ahmadi Rastegar, D. & Dzamko, N. Leucine Rich Repeat Kinase 2 and Innate Immunity. *Front. Neurosci.* **14**, 193 (2020).
16. Lin, C. H. et al. Mild Chronic Colitis Triggers Parkinsonism in LRRK2 Mutant Mice Through Activating TNF-alpha Pathway. *Mov. Disord.* **37**, 745–757 (2022).
17. Murray, P. J. Macrophage Polarization. *Annu. Rev. Physiol.* **79**, 541–566 (2017).
18. Murray, P. J. et al. Macrophage activation and polarization: nomenclature and experimental guidelines. *Immunity* **41**, 14–20 (2014).
19. Mosser, D. M. The many faces of macrophage activation. *J. Leukoc. Biol.* **73**, 209–212 (2003).
20. Levy, D. R. et al. The Parkinson's disease-associated kinase LRRK2 regulates genes required for cell adhesion, polarization, and chemotaxis in activated murine macrophages. *J. Biol. Chem.* **295**, 10857–10867 (2020).
21. Yan, J., Zhao, W., Yu, W., Cheng, H. & Zhu, B. LRRK2 correlates with macrophage infiltration in pan-cancer. *Genomics* **114**, 316–327 (2022).
22. Yan, J. et al. LRRK2 deficiency mitigates colitis progression by favoring resolution of inflammation and restoring homeostasis of gut microbiota. *Genomics* **114**, 110527 (2022).
23. Liddle, R. A. Parkinson's disease from the gut. *Brain Res.* **1693**, 201–206 (2018).
24. Chen, Q. Q., Haikal, C., Li, W. & Li, J. Y. Gut Inflammation in Association With Pathogenesis of Parkinson's Disease. *Front. Mol. Neurosci.* **12**, 218 (2019).
25. Qing, H., Wong, W., McGeer, E. G. & McGeer, P. L. Lrrk2 phosphorylates alpha synuclein at serine 129: Parkinson disease implications. *Biochem. Biophys. Res. Commun.* **387**, 149–152 (2009).
26. Sampson, T. R. et al. Gut Microbiota Regulate Motor Deficits and Neuroinflammation in a Model of Parkinson's Disease. *Cell* **167**, 1469–1480.e1412 (2016).
27. Liang, D. et al. Escherichia coli triggers α-synuclein pathology in the LRRK2 transgenic mouse model of PD. *Gut Microbes* **15**, 2276296 (2023).
28. Pan, H. et al. Genome-wide association study using whole-genome sequencing identifies risk loci for Parkinson's disease in Chinese population. *NPJ Parkinsons Dis.* **9**, 22 (2023).
29. Yang, Q. et al. Impairment of the trans-Golgi-Lysosomal Pathway Accelerates Dopaminergic Neuronal Senescence in LRRK2(R1627P) Rats. *Aging Dis.* **16**, 3089–3111 (2024).
30. Erben, U. et al. A guide to histomorphological evaluation of intestinal inflammation in mouse models. *Int. J. Clin. Exp. Pathol.* **7**, 4557–4576 (2014).
31. Yunna, C., Mengru, H., Lei, W. & Weidong, C. Macrophage M1/M2 polarization. *Eur. J. Pharm.* **877**, 173090 (2020).
32. Tsuji, Y. et al. Acetaminophen-Induced Rat Hepatotoxicity Based on M1/M2-Macrophage Polarization, in Possible Relation to Damage-Associated Molecular Patterns and Autophagy. *Int. J. Mol. Sci*. **21**, 8998 (2020).
33. Han, X., Ding, S., Jiang, H. & Liu, G. Roles of Macrophages in the Development and Treatment of Gut Inflammation. *Front. Cell Dev. Biol.* **9**, 625423 (2021).
34. Matsunaga, N., Tsuchimori, N., Matsumoto, T. & Ii, M. TAK-242 (resatorvid), a small-molecule inhibitor of Toll-like receptor (TLR) 4 signaling, binds selectively to TLR4 and interferes with interactions between TLR4 and its adaptor molecules. *Mol. Pharm.* **79**, 34–41 (2011).
35. Kawamoto, T., Ii, M., Kitazaki, T., Iizawa, Y. & Kimura, H. TAK-242 selectively suppresses Toll-like receptor 4-signaling mediated by the intracellular domain. *Eur. J. Pharm.* **584**, 40–48 (2008).

36. Wang, Y. et al. Toll-like receptor 4-mediated endoplasmic reticulum stress induces intestinal paneth cell damage in mice following CLP-induced sepsis. *Sci. Rep.* **12**, 15256 (2022).
37. Wang, J. et al. TAK-242 ameliorates DSS-induced colitis by regulating the gut microbiota and the JAK2/STAT3 signaling pathway. *Micro. Cell Fact.* **19**, 158 (2020).
38. Pastille, E. et al. Inhibition of TLR4 Signaling Impedes Tumor Growth in Colitis-Associated Colon Cancer. *Front. Immunol.* **12**, 669747 (2021).
39. de Guilhem de Lataillade, A. et al. LRRK2 is reduced in Parkinson's disease gut. *Acta Neuropathol.* **142**, 601–603 (2021).
40. Liu, T. C. et al. LRRK2 but not ATG16L1 is associated with Paneth cell defect in Japanese Crohn's disease patients. *JCI Insight* **2**, e91917 (2017).
41. Liu, Z. et al. The kinase LRRK2 is a regulator of the transcription factor NFAT that modulates the severity of inflammatory bowel disease. *Nat. Immunol.* **12**, 1063–1070 (2011).
42. Kalogeropulou, A. F. et al. Impact of 100 LRRK2 variants linked to Parkinson's disease on kinase activity and microtubule binding. *Biochem. J.* **479**, 1759–1783 (2022).
43. Zhang, Q. et al. Commensal bacteria direct selective cargo sorting to promote symbiosis. *Nat. Immunol.* **16**, 918–926 (2015).
44. Bellucci, A. et al. Nuclear Factor-κB Dysregulation and α-Synuclein Pathology: Critical Interplay in the Pathogenesis of Parkinson's Disease. *Front. Aging Neurosci.* **12**, 68 (2020).
45. Dutta, D. et al. Selective targeting of the TLR2/MyD88/NF-κB pathway reduces α-synuclein spreading in vitro and in vivo. *Nat. Commun.* **12**, 5382 (2021).
46. Phillips, R. J., Billingsley, C. N. & Powley, T. L. Macrophages are unsuccessful in clearing aggregated alpha-synuclein from the gastrointestinal tract of healthy aged Fischer 344 rats. *Anat. Rec.* **296**, 654–669 (2013).
47. Limanaqi, F. et al. Alpha-synuclein shapes monocyte and macrophage cell biology and functions by bridging alterations of autophagy and inflammatory pathways. *Front. Cell Dev. Biol.* **12**, 1421360 (2024).
48. Klegeris, A. et al. Alpha-synuclein activates stress signaling protein kinases in THP-1 cells and microglia. *Neurobiol. Aging* **29**, 739–752 (2008).
49. Schonhoff, A. M. et al. Border-associated macrophages mediate the neuroinflammatory response in an alpha-synuclein model of Parkinson disease. *Nat. Commun.* **14**, 3754 (2023).
50. Kouli, A., Horne, C. B. & Williams-Gray, C. H. Toll-like receptors and their therapeutic potential in Parkinson's disease and α-synucleinopathies. *Brain Behav. Immun.* **81**, 41–51 (2019).
51. Healy, D. G. et al. Phenotype, genotype, and worldwide genetic penetrance of LRRK2-associated Parkinson's disease: a case-control study. *Lancet Neurol.* **7**, 583–590 (2008).
52. Zhang, Z. et al. LRRK2 R1628P variant is a risk factor of Parkinson's disease among Han-Chinese from mainland China. *Mov. Disord.* **24**, 1902–1905 (2009).
53. Cabezudo, D., Tsafaras, G., Van Acker, E., Van den Haute, C. & Baekelandt, V. Mutant LRRK2 exacerbates immune response and neurodegeneration in a chronic model of experimental colitis. *Acta Neuropathol.* **146**, 245–261 (2023).
54. Subbannayya, Y., Pinto, S. M., Bösl, K., Prasad, T. S. K. & Kandasamy, R. K. Dynamics of Dual Specificity Phosphatases and Their Interplay with Protein Kinases in Immune Signaling. *Int. J. Mol. Sci.* **20**, 2086 (2019).
55. Kim, B. et al. Impaired inflammatory responses in murine Lrrk2-knockdown brain microglia. *PLoS One* **7**, e34693 (2012).
56. Hakimi, M. et al. Parkinson's disease-linked LRRK2 is expressed in circulating and tissue immune cells and upregulated following recognition of microbial structures. *J. Neural Transm.* **118**, 795–808 (2011).
57. Dzamko, N. et al. The IkappaB kinase family phosphorylates the Parkinson's disease kinase LRRK2 at Ser935 and Ser910 during Toll-like receptor signaling. *PLoS One* **7**, e39132 (2012).
58. Nazish, I. et al. Abrogation of LRRK2 dependent Rab10 phosphorylation with TLR4 activation and alterations in evoked cytokine release in immune cells. *Neurochem. Int.* **147**, 105070 (2021).
59. Ahmadi Rastegar, D. et al. Effect of LRRK2 protein and activity on stimulated cytokines in human monocytes and macrophages. *NPJ Parkinsons Dis.* **8**, 34 (2022).
60. Kubo, M. et al. Leucine-Rich Repeat Kinase 2 Controls Inflammatory Cytokines Production through NF-kappaB Phosphorylation and Antigen Presentation in Bone Marrow-Derived Dendritic Cells. *Int. J. Mol. Sci*. **21**, https://doi.org/10.3390/ijms21051890 (2020).
61. Perez-Pardo, P. et al. Role of TLR4 in the gut-brain axis in Parkinson's disease: a translational study from men to mice. *Gut* **68**, 829–843 (2019).
62. Zhang, X. et al. Different Dose of Sucrose Consumption Divergently Influences Gut Microbiota and PPAR-γ/MAPK/NF-κB Pathway in DSS-Induced Colitis Mice. *Nutrients* **14**, https://doi.org/10.3390/nu14132765 (2022).
63. Leung, H. K. M. et al. Zearalenone attenuates colitis associated colorectal tumorigenesis through Ras/Raf/ERK pathway suppression and SCFA-producing bacteria promotion. *Biomed. Pharmacother.* **164**, 114973 (2023).
64. Gao, X. et al. Correlations between α-Linolenic Acid-Improved Multitissue Homeostasis and Gut Microbiota in Mice Fed a High-Fat Diet. *mSystems* **5**, https://doi.org/10.1128/mSystems.00391-20 (2020).
65. Huang, B. et al. Babao Dan alleviates gut immune and microbiota disorders while impacting the TLR4/MyD88/NF-κB pathway to attenuate 5-Fluorouracil-induced intestinal injury. *Biomed. Pharmacother.* **166**, 115387 (2023).
66. Romano, S. et al. Meta-analysis of the Parkinson's disease gut microbiome suggests alterations linked to intestinal inflammation. *NPJ Parkinsons Dis.* **7**, 27 (2021).
67. Zhang, X., Tang, B. & Guo, J. Parkinson's disease and gut microbiota: from clinical to mechanistic and therapeutic studies. *Transl. Neurodegener.* **12**, 59 (2023).
68. Heeney, D. D., Gareau, M. G. & Marco, M. L. Intestinal Lactobacillus in health and disease, a driver or just along for the ride? *Curr. Opin. Biotechnol.* **49**, 140–147 (2018).
69. Wang, S. P. et al. Pivotal Roles for pH, Lactate, and Lactate-Utilizing Bacteria in the Stability of a Human Colonic Microbial Ecosystem. *mSystems* **5**, https://doi.org/10.1128/mSystems.00645-20 (2020).
70. Wang, X. et al. Sodium oligomannate disrupts the adherence of Rib(high) bacteria to gut epithelia to block SAA-triggered Th1 inflammation in 5XFAD transgenic mice. *Cell Discov.* **10**, 115 (2024).
71. Mihaila, D. et al. The oral microbiome of early stage Parkinson's disease and its relationship with functional measures of motor and non-motor function. *PLoS One* **14**, e0218252 (2019).
72. Barichella, M. et al. Unraveling gut microbiota in Parkinson's disease and atypical parkinsonism. *Mov. Disord.* **34**, 396–405 (2019).
73. van Kessel, S. P. et al. Gut bacterial tyrosine decarboxylases restrict levels of levodopa in the treatment of Parkinson's disease. *Nat. Commun.* **10**, 310 (2019).
74. Queipo-Ortuño, M. I. et al. Gut microbiota composition in male rat models under different nutritional status and physical activity and its association with serum leptin and ghrelin levels. *PLoS One* **8**, e65465 (2013).
75. Kunze, W. A. et al. Lactobacillus reuteri enhances excitability of colonic AH neurons by inhibiting calcium-dependent potassium channel opening. *J. Cell. Mol. Med.* **13**, 2261–2270 (2009).
76. Paillusson, S., Clairembault, T., Biraud, M., Neunlist, M. & Derkinderen, P. Activity-dependent secretion of alpha-synuclein by enteric neurons. *J. Neurochem* **125**, 512–517 (2013).

Acknowledgements

This work was supported by Key Area R&D Program of Guangdong Province (2018B030337001), National Natural Science Foundation of China

(82101657) and The National Key R&D Program of China (2021YFC2501200, 2018YFC1312001). We would like to express our gratitude to the M.D. Chenghua Yuan from Department of Neurosurgery Laboratory and M.D. Wentong Mei from Department of General Surgery Laboratory at Xuanwu Hospital, Capital Medical University for their guidance on some experimental processes. We would like to express our gratitude to the FigDraw platform. The graphical abstract was created with www.figdraw.com. Copyright Code: ATWRP5ab2a.

Author contributions

S.P., Q.Y. and P.C. participated in the design of the experiment. S.P. conducted most of the experiments, performed the data analysis, and made major contributions to the manuscript writing. Z.Y., Q.Y. and P.C. edited the manuscript. Q.Y. and Y.W. participated in the experimental sample collection. C.Z. contributed to the flow cytometry experiments. J.L. contributed to 16S rRNA analysis. C.Y. contributed to the RT-qPCR experiments. All authors read and approved the final manuscript.

Competing interests

The authors declare no competing interests.

Additional information

Supplementary information The online version contains supplementary material available at https://doi.org/10.1038/s41531-026-01281-3.

Correspondence and requests for materials should be addressed to Qiumei Yang or Piu Chan.